Alkali chloride induced superheater corrosion – Impact of percentage of molten phase

Master's thesis

Åbo Akademi University

Faculty of Science and Engineering

Ebba Malm

Matriculation number: 40058-309-2015

2021

Thesis supervisors: Docent Markus Engblom and DSc Emil Vainio

Abstract

World energy consumption has doubled in the last thirty years, and projections indicate that the energy demand will increase. Carbon dioxide is the most critical greenhouse gas generated by human activity, originating predominantly from fossil fuels, such as coal and oil. Reducing global warming has become a major goal for the next few decades. One possible solution to this problem is switching from fossil fuel to renewable fuels, such as biomass. From an environmental point of view, biomass is considered a carbon dioxide-neutral fuel as long as it is utilized in a sustainable manner.

However, the shift from fossil to biomass fuels has introduced challenges to boiler operation and efficiency. Compared to fossil fuels, biomass is an inhomogeneous fuel, and the properties and qualities of different biomasses vary a lot depending on the growth area, seasonal variations, fertilizers, etc. Biomasses may contain considerable amounts of chloride and potassium, all known to have a detrimental impact on the lifetime of the superheater material. In addition to this, black liquor also consists of inorganic chemicals from the pulping process.

Alkali chlorides on superheater surfaces may cause serious fouling and corrosion problems. One major challenge in the recovery boiler is the molten salt corrosion of the heat exchange tube material, which limits the steam temperature and boiler efficiency of the boiler. Due to high-temperature corrosion, steam outlet temperatures have been kept lower than the corresponding coal-fired boilers. In black liquor recovery boilers is steam temperature typically below 500 °C, due to the presence of molten alkali salts. Lower steam temperatures lead to lower electrical power output. As a general perception, increasing steam temperature by 10 °C, increases the power production by approximately 2%.

The focus of this work was to investigate the role of melt amount on superheater corrosion in Kraft recovery boilers. The purpose is to obtain a better understanding of the role of the amount of melt on corrosion, for the purpose of increasing the steam temperatures of the boiler. The chemical composition of the melt is only shortly discussed in this work.

The experimental part of this work consists of a laboratory corrosion study where three superheater materials were exposed to five tailor-made well-characterized synthetic alkali salt deposits. The synthetic alkali salts, containing sodium, potassium, sulfate, chlorine, and carbonate, were composed so that their first melting temperature (T_0) was the same for all cases,

but the amount of molten phase varied. Each steel/salt combination was exposed to temperatures above and below T_0 to see the significance of the molten phase at corrosion.

The chemical composition of the salts was planned and calculated based on thermodynamic calculations with the software Factsage 7.3 using the FTpulp database to obtain a well-characterized salt mixture with specific melt fraction and composition. The chemical composition of the produced salts was analyzed with SEM-EDX and Ion Chromatography and thermodynamic calculations were done based on the data from the SEM analysis, to check the melting behavior of the produced salts. The corrosion products were analyzed by means of scanning electron microscopy with energy-dispersive X-ray spectroscopy (SEM-EDX).

The results showed that the melt amount had a clear impact on high-temperature corrosion of the superheater steels. The results showed that corrosion did also, to a lesser extent, take place below T_0, but oxide layer thickness remained almost the same even though the amount of chlorine increased in the salt deposit.

The corrosion tendencies of the steel types varied. The results showed that the composition of the steels had a significant impact on corrosion resistance. The melt amount had a clear effect on corrosion layer thickness for 10CrMo and Sanicro 28, while Alloy 625 withstood corrosion up to the maximum tested melt fraction (20 wt-% melt) in this study. This work presents specific ranges for the corrosion layer thickness to better compare the corrosion of the alloys. These ranges are based on the practical experience where 20 µm/week corrosion layer thickness in laboratory-scale corresponds to unacceptable corrosion in actual boiler conditions. In this work is corrosion defined as "significant corrosion" when the mean corrosion layer thickness exceeds 20 µm/week.

Based on the corrosion layer thickness results, significant corrosion was observed both above and below T_0 for the low-alloy steel, 10CrMo9-10. While the austenitic stainless steel, Sanicro 28, showed better corrosion resistance against the molten salt corrosion. No significant corrosion was observed up to 4 wt-% melt, while the tests with a melt fraction of 6 wt-% - 10 wt-% showed low corrosion, and Sanicro 28 at 20 wt-% melt fraction exhibited significant corrosion. The nickel-based alloy, Alloy 625, exhibited good corrosion resistance and produced only a 4 µm mean oxide layer thickness at the surface of the alloy.

The tailing distribution curves were observed for Sanicro 28 at 2, 4, 6 wt-% melt. The tailing distribution curves indicate that local corrosion was a common corrosion behavior at the lower melt fractions for this steel. Furthermore, a more uniform corrosion layer was observed on the

surface of the Sanicro 28 exposed to the highest melt fraction, 20 wt-% melt. The oxide scale on 10CrMo9-10 steel was typically observed in the form of multiple thin separated layers of corrosion product, which is a typical corrosion behavior for the iron-based ferritic steels. Finally, no grain boundary attack was observed beneath the steel surface for the tests in this study.

Preface

This Master's thesis is funded by the Finnish Recovery Boiler Committee (Soodakattila yhdistys) and conducted at the Laboratory of Inorganic Chemistry at Åbo Akademi University. I would like to thank Soodakattila yhdistys for this opportunity and especially big thanks to Johanna Tuiremo for giving her expert advice on some parts of the work.

I would like to thank my supervisor Markus Engblom for his guidance, patience, and support both when it comes to the writing process and also for all the help I have received while preparing presentations. Also, a big thanks to Emil Vainio for helping with everything from the thermodynamic calculations to providing valuable insights related to the research. I am very grateful for all the help and support, and our discussions has been truly inspiring during the process! I also want to thank other OOK members that have been important along the way: Juho Lehmusto, Patrik Yrjas and Elisa Hupa, for all the feedback, comments, and great ideas during our brainstorm meetings. Your input has been extremely helpful! Also big thanks to, Jaana Paananen for supporting me during the laboratory work, and Linus Silvander for conducting all the SEM analysis for me. Thank you for always being so kind and supportive!

Finally, I would like to thank my dear family for all the love and support that I so unconditionally have received throughout the years. Thank you for believing in me and cheering on me no matter what I have been doing! Furthermore, I am incredibly thankful for all the wonderful friends that I am so lucky to have by my side along this journey. An extra big thanks to one special person, for all the inspiring words and for always telling me "Allt blir alltid bra!". I appreciate you!

Tammerfors, 03.05.2021

Ebba Malm

Abbreviations

FMT/ T_0 = First Melting Temperature

IC = Ion Chromatography

SE = Secondary Electrons

BSE = Backscattered Electrons

SEM-EDX = Scanning Electron Microscope-Energy Dispersive Spectroscopy

Table of Contents

Svensk sammanfattning

Under de senaste decennierna har det observerats en radikal ökning av energibehov runt om i världen och projektioner indikerar att energibehovet kommer att fortsätta öka. Utöver detta ökar även människans utsläpp av växthusgaser till atmosfären. Koldioxid är den mest kritiska växthusgasen som orsakas av människans aktivitet på planeten och den härstammar i huvudsak från förbränning av fossila bränslen. Vid klimattoppmötet i Paris kom deltagarna i mötet överens om ett gemensamt mål att hålla temperaturökningen väl under två grader jämfört med förindustriell tid. För att detta mål skall vara möjligt krävs en lösning på de utmaningar och problem som energiproduktionen möter. En möjlig lösning vore att övergå från förbränning av fossila bränslen till att förbränna biomassa, så att den totala mängden koldioxid som släpps ut skulle minska. När det kommer till koldioxidutsläpp anses biomassa vara ett koldioxidneutralt bränsle eftersom plantor konsumerar samma koldioxid mängd under deras tillväxtperiod som avges när de förbränns.

Däremot, så uppstår det många material relaterade problem i värmepannor där biomassa används som bränsle. Ur ett kemiskt perspektiv är biomassa ett inhomogent bränsle, som vanligtvis innehåller hög koncentration vatten och en ansenlig mängd kalium och klorid. Dessa element är kända för att accelerera beläggningen och korrosionen av stålmaterialet i värmeöverförarna hos värmepannor.

Elementen i biomassan frigörs som rökgas eller aska under förbränningen. Dessa föreningar förs upp med rökgasen till den övre delen av pannan där överhettarna är placerade och där kondenseras föreningarna på överhettarnas metallyta. Dessa alkaliföreningar har låg smältpunkt, vilket är orsaken till att de flesta av sodapannornas ångtemperaturer är begränsade till runt 480 °C. Denna ångtemperatur är avsevärt mycket längre än 540 °C som är den ångtemperatur som konventionella kolkraftverk opererar med.

Som en lösning på detta problem har ångtemperaturen in värmepannorna hållits på en låg nivå, vilket resulterar i en minskning av kraftverkets effekt. En 10 °C temperaturhöjning av ångan skulle resultera i 2 % ökning av kraftverkets effekt. Därför behövs det mera effektiva sätt att motverka korrosionen så att kraftverk som utnyttjar biomassa kan höja ångtemperaturen och bli mera effektiva och konkurrera med fossila bränslen.

Från en materialingenjörs perspektiv skulle problemet bemötas genom att modifiera den kemiska sammansättningen och legeringsmetallerna i överhettarmaterialet för att förbättra

stålet korrosionsresistans, medan kemi-ingenjörer skulle fokusera på att studera askans och rökgasens sammansättning och smältegenskaper.

När det kommer till att välja ett passande överhettarmaterial är det två faktorer som inverkar på beslutet: omgivningens egenskaper och materialkostnaden. Omgivningens egenskaper såsom den omgivande temperaturen, rökgassammansättning och koncentration vatten är viktiga faktorer när det kommer till att välja material. Men utöver detta är även priset en viktig faktor i processen, eftersom längden på överhettarrör som används till en anläggning mäts i kilometerskala. I mindre korrosiva processer och vid lägre temperaturer används generellt låglegerade järnbaserade stål pga. av deras förmånliga pris. Dessa järn-baserade stål innehåller mindre än 5 % av krom, nickel och molybden. I detta arbete har 10CrMo9-10 använts för att representera denna kategori.

En legerings korrosionsbeständighet kan förbättras genom att tillägga krom till metallegeringen. Vid en kromkoncentration på över 10 vikt% reagerar krom med syre i luften, och bildar ett skyddande oxidlager på stålytan. När krom adderas till ett järn-baserat stål så förbättras stålets egenskap att motstå korrosion och så bildas så kallat rostfritt stål. Metallstrukturen hos rostfritt stål kan antingen vara ferritisk struktur eller austenitisk struktur. Den austenitiska stukturen är naturligt stabil endast under höga temperaturer, och genom att tillägga nickel så stabiliseras strukturen även under låga temperaturer. De austenitiska rostfria stålen innehåller mera än 16 vikt% krom och tillräckligt hög koncentration nickel för att stabilisera austenitiska strukturen. Priset på nickel är högt så det relativa priset på austenitiskt stål kan vara upp till tre gånger så högt som det låglegerade ferritiska stålet (10CrMo9-10). Det austenitiska stålet Sanicro 28 som studerats i detta arbete har valts ut att representera denna kategori.

Värmeöverföringsmaterialet som används i mera korrosiva miljöer är generellt nickel-baserade metaller. Trots deras överlägsna egenskaper så används de inte i så stor utsträckning pga. det höga priset på nickel. I detta arbete har den nickelbaserade legering Alloy 625 valts ut att representera denna kategori.

Målet med detta arbete var att lära sig mera om överhettarkorrosionen i en sodapanna, med mera fokus på betydelsen av mängden smälta i förbränningsaskan. Till korrosionsexperimenten i detta arbete användes fem skräddarsydda alkalisalter och tre överhettarstål (10CrMo9-10, Sanicro 28 och Alloy 625). Alkalisalterna, innehållandes natriumsulfat Na_2SO_4, kaliumsulfat K_2SO_4, natriumklorid NaCl, natriumkarbonat $NaCO_3$, hade komponerats ihop så att de har

samma första smältpunkt, T_0, men mängden smälta vid T_0 varierar för varje fall. I detta arbete undersöktes reaktionsmekanismerna mellan smältamängderna och olika stål. Till experimenten, som utfördes i laboratorium, utnyttjades horisontella ugnar och analytisk utrustning (SEM/EDX, jonkromatografi, termodynamiska uträkningar). Korrosionsexperimenten utfördes för varje stål-salt-kombination vid två temperaturer: över T_0 vid 560 °C och under T_0 vid 520 °C.

Resultatet i detta arbete visade på att smältamängden hade en signifikant inverkan på korrosion av överhettarmaterial. Man kunde också observera att korrosionen skiljde från metall till metall, så därför kunde man konstatera att stålens sammansättning spelade en stor roll i förmågan att motstå korrosion. Hos korrosionsexperimenten som var utförda över T_0 så kunde man observera att oxidskiktets tjocklek ökade när smältamängden i saltet ökade, medan under T_0 kunde man klart se att det inte skedde någon ökning i korrosion baserat på den beräknade oxidskiktets tjocklek. Detta innebär att även fast mängden klorid ökar i beläggningen så ökar inte korrosionen mycket så länge mängden smälta i beläggningen hålls låg. Detta skulle indikera att smältamängden har en stor roll i korrosionsprocessen. Resultatet visade också att den nickel-baserade stålet motstod korrosion bäst, således är stålets sammansättning en viktig faktor när det kommer till att en smälta är närvarande.

Introduction and objective

Over the last decade, the atmospheric concentration of key greenhouse gases has increased due to human activity. According to the climate change report from 2007 is carbon dioxide the most important anthropogenic greenhouse gas in the atmosphere (Pachauri & Reisinger, 2008). The carbon dioxide concentration was recently measured at NOAA's Mauna Loa Observatory in Hawaii to nearly 412 ppm, which represents a 47% increase compared to pre-Industrial time (Alan Buis, 2019). The burning of fossil fuels, such as coal and oil, is the main anthropogenic activity that releases carbon dioxide into the atmosphere. Global warming can be reduced by reducing the contribution of greenhouse gas emissions to the atmosphere. (Wong, 2015) Although global warming awareness has increased among people, the problems and challenges that the emission reduction requires are far from solved.

The inhibition of global warming has become an essential target for the coming decade. The Paris agreement's stated objective to keep global temperature rise well below 2 degrees Celsius pre-industrial levels requires a reduction of greenhouse gases in the atmosphere to prevent anthropogenic interference with the climate system. An essential strategy is to replace fossil fuels with alternative fuels such as renewable fuels. Biomass is one alternative among renewable energy sources. The main advantage of biomass is that it is considered a carbon dioxide-neutral fuel if it is utilized sustainably. Photosynthesis removes CO_2 from the atmosphere during the growth of biomass, and the same amount of CO_2 is released back to the atmosphere during combustion.

Although biomass is a promising alternative to fossil fuels, it does not come without challenges. The characteristic properties of biomass as a fuel introduce several challenges and problems to the boiler operation. For instance, biomass is an inhomogeneous fuel with high water concentration and varying chemical composition. The complex composition makes it difficult to predict its behavior during combustion in terms of ash formation. Biomass contains a considerable amount of chlorine and potassium, which both are known to contribute to deposit formation and superheater corrosion. (Hansen et al., 2000) Potassium chloride deposits onto the surfaces of superheater tubes and increases the oxidation of the steel surface (Grabke et al., 1995).

Deposits containing alkali chlorides have a relatively low melting temperature, which is why most recovery boilers operating today run at low steam temperatures. The newest recovery boilers run at a steam temperature around 500 °C. This temperature is significantly lower than

a conventional coal-fired power plant, which usually operates at steam temperatures above 540 °C. Besides decreasing the boiler efficiency, the deposits also cause unscheduled shutdowns of the boiler in the most severe cases. The unscheduled shutdowns of the boiler decrease the boiler availability, causing economic losses to the pulp mill. Increasing steam temperature and pressure to 520 °C and 104 bar would increase the power production by 7%. (Bajpai, 2017) Therefore, the one major effort in high-temperature corrosion research is to protect materials from the attack, so that biomass-fired boilers can operate at higher temperatures. From a material point of view, the approach is to modify the chemical composition and alloying elements in the steel material to improve the corrosion resistance of the material. Simultaneously, the chemical engineers study the flue gas and fly ash and their respective composition and melt behavior.

The high chlorine and potassium contents in many biomasses are harmful elements considering superheater corrosion. The most severe corrosion attacks are associated with Cl-rich deposits formed on the superheater tubes. Additionally, when the superheater steel surface temperature becomes high enough, the ash-deposit begins to melt, further enhancing the oxidation of the surface. Potassium chloride forms low-melting eutectics with other elements in the flue gas and fly ash. (Nielsen et al., 2000) To prevent chloride-induced corrosion, the steel temperature can either be kept low or a more corrosion-resistant material can be utilized.

There are different kinds of steel types available on the market with a variety of corrosion resistance. The corrosion resistance of steel depends on the chemical composition and the crystal structure. For instance, the addition of chromium increases the corrosion resistance of an alloy, because chromium oxidizes and form a protective chromium oxide layer on the steel surface. To further improve the corrosion resistance, the crystal structure of the metal can be shifted to an austenitic structure. This structure is stable when adding a so-called austenite stabilizer, for instance, nickel.

However, material selection is also vastly dependent on the material price. For instance, the relative cost of nickel-based alloys is as much as three times higher than the iron-based, low-alloy, steels. In this work, three superheater material are chosen to represent some of the alloy categories: 10CrMo9-10 represents the category of low-alloy ferritic steels, Sanicro 28 represents the category of austenitic stainless-steels and the third alloy is Alloy 625, which is the most corrosion-resistant alloy in this work and represents the category of nickel-based alloys.

The objective of this work is to obtain a better understanding about how corrosion of superheater materials depends on the amount of melt present.

- Three steels tested in exposure to five different synthetic salts with different Cl content.
- The T_0 of the salts are the same, but the amount of melt formed at or near the first melting point T_0 is different.
- Each salt/steel combination was exposed to two temperatures, a temperature below T_0 (520 °C) and above T_0 (560 °C).

Background

The Kraft chemical process is the dominating pulping process globally, due to the superior strength properties of the pulp and because of the economic benefits of the process. Compared to mechanical pulping, this process produces high-quality fibers that are long and durable.

In the chemical pulping process, wood chips are mixed with inorganic chemicals to react. The inorganic chemicals, Sodium sulfide (Na_2S) and hydroxide (OH^-) dissolve the complex organic glue that binds the cellulose fibers together. Some of the organic compounds in the wood chips oxidize to carbonate, and some of the sulfides in the inorganic chemicals oxidize to sulfates. The pulp fibers are removed for further processing into paper, leaving a solution of inorganic cooking chemicals, lignin, and other organic matter from the wood behind. This by-product is the weak black liquor. The initial concentration of weak black liquor is about 15% dry solids in water. The weak black liquor is concentrated in evaporators to a dry solid content between 65% and 85% for combustion. (Adams et al., 1997) As the dry solid concentration increases, the black liquor becomes more viscous, and the boiling point rises (Green et al., 1992). The Kraft recovery boiler is a steam generator that combusts the evaporated black liquor to generate high-pressure steam for energy production. (Green et al., 1992)

The recovery process has two functions, to regenerate the inorganic pulping chemicals, NaOH and Na_2S, and to produce high-pressure steam to provide energy to the pulp mill. (Tran & Vakkilainen, 2008) The pulp industry combusts 200 million tons of black liquor dry solids every year, making it the fifth most important fuel globally, next to coal, oil, gasoline, and natural gas. The chemical pulping process is self-sufficient since, in most cases, the heat and energy generated from the combustion process are enough to run the whole pulp mill. (Cheremisinoff & Rosenfeld, 2010) Today, the Kraft pulp mill regenerates up to 98% of the process chemicals. (Bajpai, 2017)

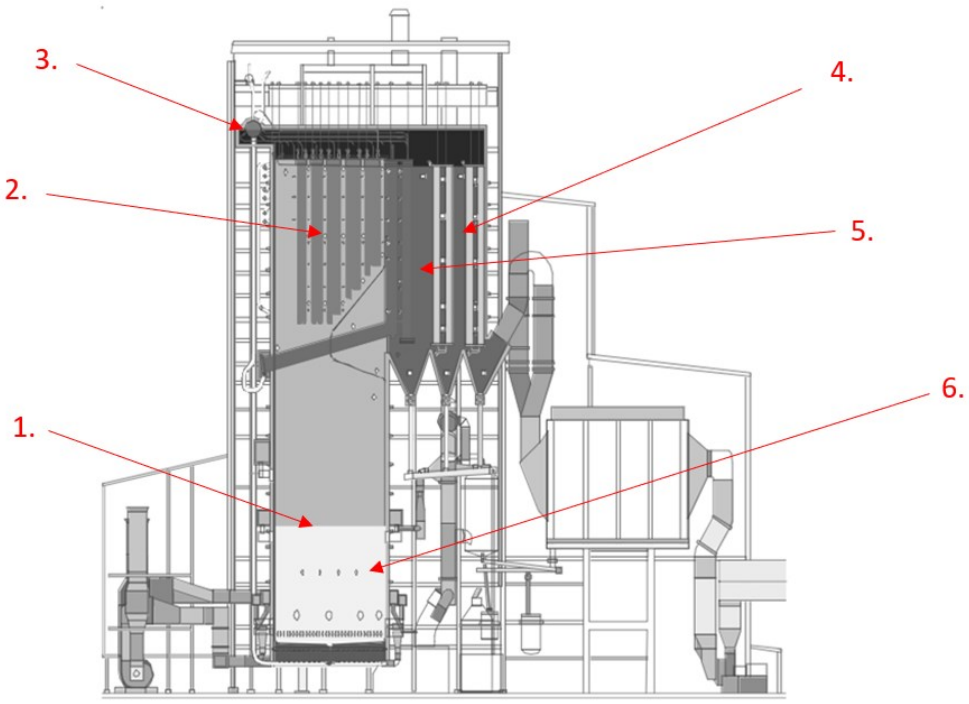

Figure 1. The world's largest recovery boiler at Jinhai Pulp &Paper, Hainan. 1. Furnace 2. Superheaters 3. Steam drum 4. Economizer 5. Feedwater from tank 6. Liquor guns and tertiary airports. (Soodakattilayhdistys, 2009) (Haaga et al., 2002)

However, the electrical output of the chemical recovery process is limited due to the complex chemical processes in the furnace. The elements in the black liquor and inorganic chemicals causes ash-related issues in the boiler operation. In addition to this, as modern mill operations are shifting into more closed systems to minimize the generated amount of waste, subsequently leading to a substantial increase in non-processed elements, such as potassium and chlorine, which are known to contribute to the ash-related issues in the boiler (Adams et al., 1997). The following section will address the ash-formation processes inside the furnace.

Ash behavior

Black liquor

The main focus in this work is on black liquor and the black liquor recovery boiler ash chemistry, but many of the principles are also applicable to other biomass-based fuels.

Understanding the fuel characteristics is necessary when studying the ash behavior of black liquor. The chemical composition directly impacts the combustion gas and fly ash**.** Black liquor contains very fine organic compounds and inorganic chemicals from the pulping process, and a high concentration of water. The characteristics of black liquor as a fuel are very different from fossil fuels, including moisture content, ash content, calorific value, and alkali metal content.

Alkali salts are the source of many challenges inside biomass-fired boilers, because they cause severe corrosion and fouling to the superheater surface of the boiler. Black liquor has a much higher potassium (K) concentration and significantly higher chlorine (Cl) concentration than many other fuels, such as coal and oil. A relative amount of chloride and potassium are released into the gas phase during the combustion, resulting in a high concentration of alkali salt ash particles in the flue gas. (Mikkanen et al., 1999) The alkali-containing compounds are responsible for many of the ash-related issues in the recovery boiler.

The ash composition is directly dependent on the fuel species, therefore, the same alkali-containing compounds are also encountered during the combustion of biomass, since black liquor originates from biomass. The superheaters inside the furnace are mostly affected by alkali-induced slagging, decreasing the heat transfer which further reduces the boiler efficiency. (Niu & Tan, 2016)

The composition of black liquor varies from mill to mill and within the same mill. (Green et al., 1992) Table 1 presents a typical chemical composition of a black liquor.

Table 1. Elemental composition of black liquor

Component	wt-%
Carbon	34-39
Hydrogen	3-5
Sulfur	3-7
Oxygen	33-38
Chloride	0.2-2
Potassium	0.1-2
Sodium	17-25
Nitrogen	0.04-0.2
Other	0.1-0.3

Combustion processes inside the furnace

Black liquor combustion generates alkali-containing vapors. Potassium and chlorine are among the most common ash-forming elements in many biomass fuels (Adams & Frederick, 1988) The combustion process of black liquor droplets in the furnace occurs in four chemical stages. These are drying, pyrolysis, char oxidation, and smelt reactions. Liquor guns, located in the lower furnace above the secondary air, spray black liquor into the furnace as tiny droplets. When a fuel droplet enters the furnace, its temperature quickly rises, and water vapor is released; consequently, the particle dries. When the droplet has dried entirely, and when the liquor solid reaches a temperature of about 200 °C, pyrolysis reactions start. Small amounts of potassium are bound to the organic structure within the biomass. This structure decomposes at low temperatures of volatile combustion (300-500 °C), resulting in the release of potassium into the gas phase. During this stage, also much of the carbon, hydrogen, sulfur, and nitrogen in the black liquor solids are released.

Primary reactions can release potassium during devolatilization, and secondary reactions during char combustion (Werkelin, 2008). Potassium chloride has a higher vapor pressure than sodium chloride and is more easily released into the gas phase.

During char burning stage, and some of the sodium, potassium, chloride, and sulfur are vaporized to the gas phase to form HCl and alkali chlorides (Adams et al., 1997). Previous studies indicate that the major sodium and potassium release occurs during the char combustion stage of the combustion process of black liquor (Verrill, 1992).

The transportation of ash to the superheater area depends greatly on the droplet volume. There are two types of fly-ash particulates: carryover and fume. The focus of this work will be on the fume particles rather than the carryover particles. The fume particles are much smaller than carryover particles, and their size ranges from 0.1 to 1 μm. Fume formation consists of two major stages, first the volatilization of sodium and potassium compounds at high temperatures in the lower part of the furnace, and second condensation of these compounds on the colder superheater surface in the upper part of the furnace, initiating a deposit build-up. (Lindberg et al., 2007). (Adams et al., 1997) The composition of fume depends strongly on the amounts of sodium and potassium released during the char combustion stage. The following chapter will further discuss the melting behavior of the black liquor ash.

Ash melting behavior

The melting behavior of the ash deposits is an important factor to take into considerations when investigating corrosion of superheater steels. The mixture of components coming from flue gas or fly ash forms complex low-melting eutectic mixtures that cause detrimental material degradation. The melting behavior of a salt deposit depends on the composition of elements and their chemical interactions, and typically, deposits do not have a specific melting point. Instead, melting occurs within a broad temperature range. These kinds of mixtures are also referred to as eutectic mixtures. The definition of a eutectic mixture is a homogeneous mixture of two or several components, which do not interact and form a new chemical compound. However, a specific ratio of the elements inhibits the crystallization path so that the melting point of the mixture is lower than the melting point of the individual constituents. The formation of low-melting eutectic mixtures is detrimental to the boiler operation and contributes to severe fouling and corrosion problems.

As previously mentioned, potassium and chlorine are two elements that have an important role in the melting behavior of ash and these elements are commonly present in biomass fuels. Shinata proposed that eutectic melts of sodium chloride and sodium chromate enhance the corrosion rate. The eutectic mixture that forms is partly molten at typical boiler temperatures. The melting point for these eutectic mixtures ranges from 200 to 600 °C. (Spiegel, 1999)

The melt is believed to work as an electrolyte for the electrochemical reaction and is, therefore, accelerating the corrosion. Additionally, the melt formation is also believed to hinder the formation of the protective oxide. (Shinata, 1987)

The melting behavior of the deposits in black liquor boilers are mainly governed by chlorine, potassium, carbonate, and sulfide content. The first melting temperature is especially important from the corrosion point of view since previous studies have shown that corrosion increases as the FMT of the deposit is exceeded. The estimation of melting curves of salt mixtures is done based on a multiphase equilibrium model to predict the chemistry of the ash forming elements in the black liquor combustion.

A small amount of chlorine present in the ash deposit will decrease the first melting temperature, T_0. When chlorine is present in the deposit, a further increase of chlorine content to the salt mix will not affect T_0 because of the eutectic nature of the mixture. The addition of chlorine will, however, increase the melt fraction of the salt. On the other hand, the addition of potassium, to an alkali salt that already contains chlorine, will decrease the first melting

temperature (T_0) further. However, the addition of potassium to a non-chlorine-containing alkali salt does not affect the T_0 and potassium does not affect the amount of melt formed at T_0. (Skrifvars et al., 2008) (Salmenoja, 2000)

Table 2 presents the melting temperatures for some alkali salt deposits typically encountered in a biomass-fired boiler. Potassium chloride forms low-melting eutectics with $FeCl_2$ and $CrCl_2$ at temperatures of 360 and 470°C, respectively. KCl forms an even lower melting eutectic with $FeCl_3$. Additionally, KCl and NaCl also form more complex eutectic mixtures together with the corrosion products and intermediate components that form on the steel surface. Sodium chromates can form as an intermediate in high sodium chloride concentrations. Sodium chromate and sodium chloride form a low melting eutectic mixture. According to Shinata, sodium chromate formation decreased the melting temperature from about 800 ℃ to approximately 560 ℃ (Shinata, 1987).

The ash melting behavior is also important when it comes to deposit build-up, and this problem will be further discussed in the following chapter.

Table 2. Melting temperature of components commonly encountered at the superheaters. (Nielsen et al., 2000)

Components	Melting temperature (°C)
NaCl	801
KCl	770
$FeCl_2$	677
$CrCl_2$	845
KCl – $FeCl_2$	340 – 393
KCl – $FeCl_3$	~202
KCl – $CrCl_2$	462 – 475
NaCl – $CrCl_2$	437
KCl – K_2CrO_4	650
NaCl – Na_2CrO_4	557

Deposit formation

The deposit formation of fly ash depends greatly on the stickyness of the ash. The alkali chlorides form low melting eutectics with other alkali compounds, increasing deposit build-up. The fly ash particles melt behavior was studied by Backman et al. in 1987. The study concluded

that for a particle to be considered sticky, it must have a liquid content that exceeds 15%, below that temperature, the particle is considered “dry”, and therefore it does not adhere to the tube surface. However, a liquid concentration above 70% particle contains too much liquid so that the particle will drop off the surface. (Backman et al., 1987)

Deposit formation is illustrated mechanistically in figure 2. Salt particles from the flue gas adhere to the metal surface, forming the initial deposit layer. By the reaction of the salt particles, flue gas, and metal, complex corrosion products with lower melting temperatures can form. The partly molten corrosion products may further accelerate the build-up of the deposit (Cha & Spiegel, 2006).

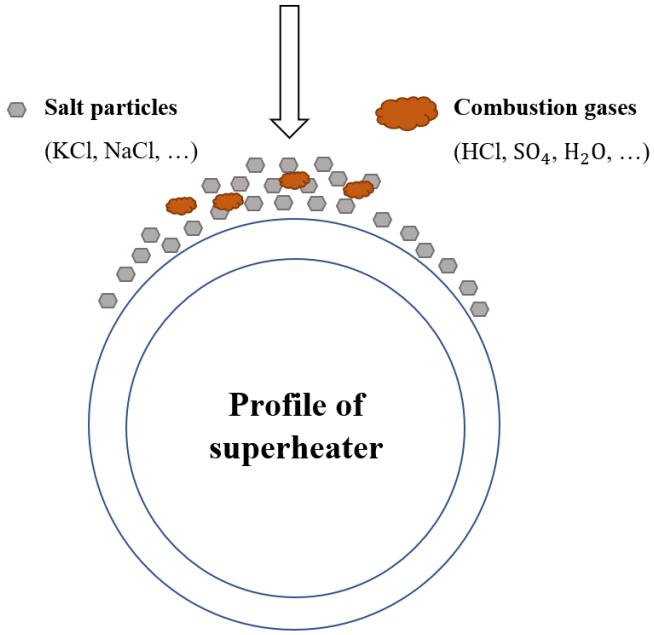

Figure 2. Illustration of the deposit formation of the superheater tube. (Cha & Spiegel, 2006)

Corrosion products

Most metals are thermodynamically unstable in oxygen and at high temperatures. Metal oxides are, therefore, the most common corrosion product on the steel surface. The corrosion resistance of a metal depends on the properties of the metal oxide that forms on the steel surface. The metal can also form other compounds together with other elements in the system, for instance, metal chlorides. Metal and chlorine generally react together to form transition metal chlorides in biomass-fired boilers. The corrosion rate of the metal is influenced by the metal oxide and

the other compounds that form. The oxide formation is dependent on the temperature and thermodynamic stability of the oxides and oxygen partial pressure in the system. (Cottis, 2010)

Transition metal chlorides

The presence of KCl and NaCl in the flue gas promotes the formation of transition metal chlorides on the surface of the heat exchangers. Depending on the alloying elements in the steel material, various chlorides form, such as $FeCl_2$, $FeCl_3$, $CrCl_3$, $NiCl_2$. The presence of transition metal chlorides generally causes severe corrosion and it also makes it difficult for the oxide scale to adhere to the steel surface. Metal oxides are the stable components at the recovery boiler temperatures. However, transition metal chlorides become the stable components at the metal/oxide interface due to low oxygen partial pressure. The metal chlorides subsequently oxidize as they diffuse away from the steel surface, toward higher oxygen concentrations. (Larsson, 2017)

Iron chlorides are most frequently occurring on low-alloy steels in the presence of alkali salts due to their high iron content and low chromium. Iron chloride evaporates easily at high temperatures, resulting in relatively fast material depletion of the bulk steel. (Nielsen et al., 2000)

Metal oxides

Different metal oxides can form, depending on the chemical composition of the steel and the oxygen concentration. Iron can form several forms of iron oxides, wüstite (FeO), magnetite (Fe_3O_4) and hematite (α-Fe_2O_3). The formation of these depends on several factors, such as the temperature and the oxygen partial pressure. Wüstite (FeO) forms on pure iron above 570 °C, while the FeO formation requires higher temperatures on iron alloys. Hematite is the most protective iron oxide, and in dry atmospheres, it remains protective up to 500 °C. Magnetite is less protective than hematite but more protective than the wüstite. (Kofstad, 1988)

Another typical metal oxide that generally forms on chromium-containing metal alloys is eskolite, Cr_2O_3. The eskolite oxide is the most protective oxide of the oxides that form on stainless steel and this is the main component that provides the high corrosion resistance. Eskolite is the only stable chromium oxide at higher temperatures. A minimum chromium concentration of approximately 9% is required to form a Cr-containing surface oxide in Fe-Cr steel. Steels with lower chromium concentrations form an oxide layer mainly consisting of iron oxide since chromium remains in the bulk steel. (Ropo et al., 2011)

Solid solutions form if the oxide layer consists of both chromium and iron oxides because chromium is entirely soluble in iron oxide. This solution is a corundum type solid solution (Fe, $Cr)_2O_3$, while alloys consisting of several alloying elements generally form a spinel-type solid solution $(Fe, Cr, Ni)_3O_4$ with Fe, Cr, and Ni. The composition of the oxide depends on the chemical elements in the bulk metal. (Kofstad, 1988)

Corrosion mechanisms

Some research have been made about the superheater corrosion in boilers fired with biofuels. Salmenoja reviewed the corrosion mechanisms of the Cl-induced superheater corrosion in biofuel boilers, including boilers fired with black liquor. According to Salmenoja, "Chlorine corrosion is usually related to either gaseous hydrochloric acid (HCl) formation or alkali chloride deposition on the tube surfaces." (Salmenoja, 1999). The most severe corrosion problems occur due to the formation of Cl-rich deposit on the superheater tubes and molten salt corrosion is the main corrosion mechanism (Salmenoja, 2000). This work will mainly focus on the chlorine corrosion caused by the alkali chloride deposition.

Chlorine in the form of alkali chlorides is generally known to enhance superheater corrosion (Skrifvars et al., 2010). Potassium chloride considerably lowers the FMT of the deposits in black liquor recovery, increasing the amount of melt in the deposit. At normal recovery boiler temperatures, a relatively high amount of melt can form in the black liquor recovery deposits.

The chlorine corrosion has previously been explained by a reaction mechanism called the "chlorine cycle" which involves: 1) formation of volatile metal chlorides at the steel surface, 2) diffusion of the formed chlorides through oxide scale, and 3) oxidation of chlorides at higher oxygen partial pressure. (Grabke et al., 1995) (Salmenoja, 2000)

Chlorine-induced corrosion

In oxidizing environments, the metal is oxidized and forms a dense oxide scale near the metal surface. This oxide scale barrier prevents oxygen and other gases from accessing the metal surface, preventing corrosion. Chlorine is believed to penetrate the protective oxide scale through the pores and cracks to further react with the metal, forming metal chlorides at the metal-scale surface. (Niu & Tan, 2016)

According to previous studies, potassium chloride and sodium chloride enhances the break-up of the protective oxide on the steel surface, forming chromates, K_2CrO_4, and Na_2CrO_4 leaving

an easy pathway for chloride to react with the unprotected steel surface. The formation of potassium chromates depletes the chromium from the oxide, leaving behind an iron-rich non-protective oxide. (Pettersson, J. et al., 2005)

Shinata suggested that chlorine mainly acts as a catalyst via the formation of metal chlorides at the metal/oxide surface (Shinata, 1987). Figure 3 illustrates the reaction path of the metal chloride to metal oxide.

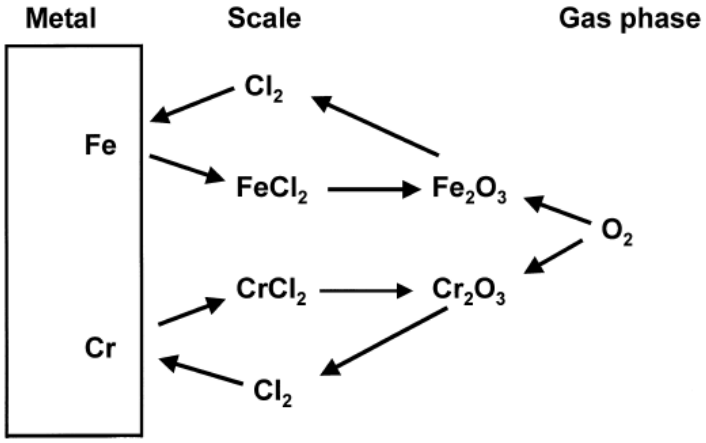

Figure 3. Illustration of the chlorine cycle (Nielsen et al., 2000)

Many corrosion studies have been carried out with synthetical boiler ash deposits containing potassium chloride and other mixed chlorides and several reaction mechanisms have been proposed for potassium chloride-induced corrosion (Nielsen et al., 2000) (Zahs et al., 2000). Despite their differences, they exhibit the same underlying principle: potassium chloride reacts with chromium oxide, leading to the destruction of the protective oxide layer, leading to the out-of-control oxidation reaction.

The next section will briefly present the general reactions that are assumed to occur in the chlorine corrosion process.

Reaction mechanisms

Initially, the KCl and NaCl are believed to react with the oxide scale of the sample forming ferrate or chromate while chlorine gas (Cl_2) is released (Spiegel, 1999). Though in most cases, enough water vapor is present, so HCl formation is thermodynamically favored over chlorine formation.

$$NaCl + Fe_2O_3 + \frac{1}{2}O_2 = NaFe_2O_4 + \frac{1}{2}Cl_2$$

$$KCl + Cr_2O_3 + \frac{5}{2}O_2 = K_2CrO_4 + \frac{1}{2}Cl_2$$

The chlorine diffuses through cracks and pores of the oxide scale to the metal/scale interface to form metal chlorides.

$$Me(s) + Cl_2(g) \rightarrow MeCl_2(s)$$

where Me represents Fe, Cr, and Ni. Due to the low oxygen concentration at the metal/scale interface, metal chlorides ($FeCl_2$ and $CrCl_2$) are thermodynamically stable. Metal chlorides have a high vapor pressure and evaporate continuously according to the equation below.

$$MeCl_2(s) \rightarrow MeCl_2(g)$$

The metal chlorides diffuse outward from the metal surface to higher oxygen partial pressure $p(O_2)$. As the oxygen concentration increases, the metal chlorides start to oxidize into solid metal oxides and Cl_2 is simultaneously released during the process, completing the chlorine cycle. (Grabke et al., 1995)

$$2MeCl_2(g) + 3O_2(g) \rightarrow 2MeO_3(s) + 4Cl_2(g)$$

$$3MeCl_2(g) + 2O_2(g) \rightarrow Me_3O_4(s) + 3Cl_2(g)$$

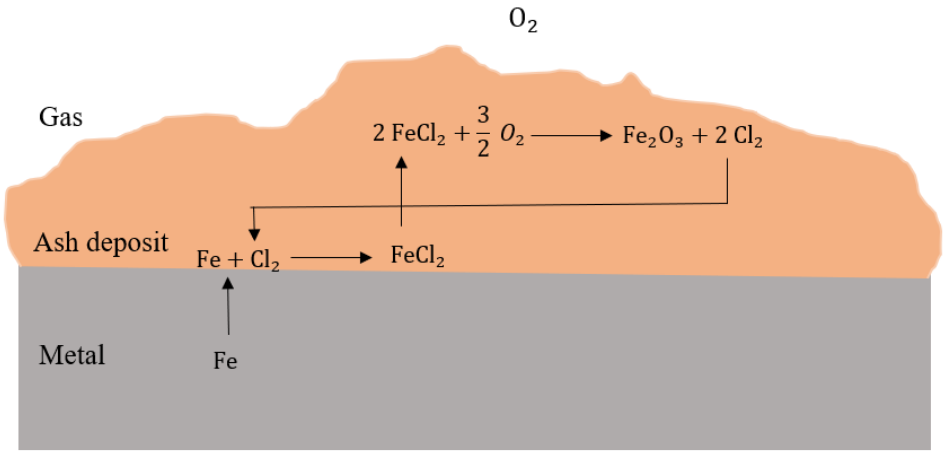

Figure 4. Model of chloride-induced high-temperature corrosion according to Grabke. Illustration after (Ropo et al., 2011).

The thermodynamic stability of the metal oxides and metal chlorides depends on oxygen concentration and chlorine concentration in the vicinity. The metal oxides are the thermodynamically stable phases at elevated temperatures. However, chlorides become stable at the metal/oxide interface due to the low oxygen concentration. A comparison of the Gibb's free energy of formation at 600 °C for different metal chlorides gives: $CrCl_2$ = −286.0 kJ/mol; $FeCl_2$ = −232.1 kJ/mol; $NiCl_2$ = −174.2 kJ/mol. According to these data, a less reactive behavior is predicted for nickel (Zahs et al., 2000).

The chlorides evaporate and diffuse up toward higher oxygen partial pressures and react with oxygen to form solid oxides. Figure 3 shows the oxygen partial pressure and temperature dependence of the formation from gaseous chlorides to solid oxides. Nickel chloride converts into oxide at very high oxygen partial pressure, iron chloride at significantly lower oxygen pressure, and low oxygen concentration is needed to convert chromium chloride into Cr_2O_3. The low required oxygen concentration means that chromium oxide forms closer to the steel surface than iron and nickel oxide. The oxide scale of low-alloy steels is typically formed as multiple thin layers of oxides. This is most likely because iron chlorides oxidize at higher oxygen concentrations, further away from the steel surface. In conclusion, the characteristic differences between the corrosion behavior are most likely caused by the different reactivities concerning chloride formation, and the oxygen partial pressure needed for conversion from gaseous chlorides into solid oxides.

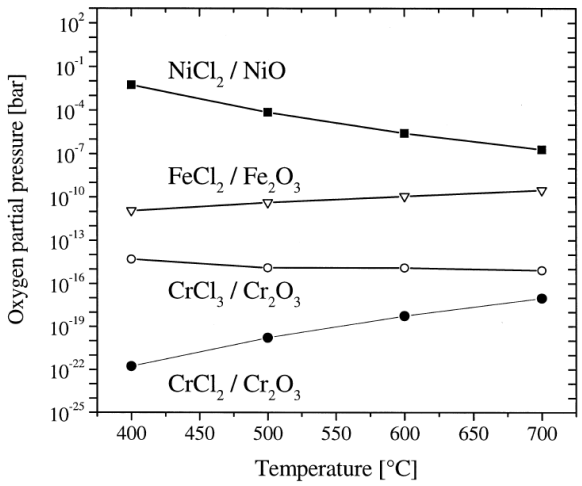

Figure 5. Equilibrium oxygen partial pressures of the reaction from gaseous chlorides to solid oxides at 400-700°C calculated from the Cl_2-activity of the gas atmosphere with 500 vppm HCl and the equilibrium vapor pressures of the metal chlorides (in bar). The image is taken from (Zahs et al., 2000).

Transportation of chlorine through the oxide scale

Initial theories have suggested that molecular chlorine diffuses through the oxide scale through the cracks and pores in the oxide scale. However, it is not fully elucidated how the chlorine (Cl_2) is transported back to the steel surface and how it penetrates the crack-free oxide scale. Additionally, suppose cracks and pores are present in the oxide scale, the same diffusion path would also be available for oxygen molecules as the size of chloride molecules is considerably larger than the oxygen molecules. (Larsson, 2017) However, it is also questionable if the reactive chlorine gas would diffuse through the oxide layer and reach the steel surface without being reduced.

Following this, Cantatore et al. suggested an alternative scenario for steel chlorination where instead of a gas phase diffusion of Cl_2 molecules, a solid-state diffusion of chloride ions would occur through the oxide layer (Cantatore et al., 2019) (Larsson, 2017). As an alternative reaction route, chlorine is suggested to penetrate the oxide scale by grain-boundary diffusion. (Pettersson et al., 2005)

The solubility of metal oxides in molten salt

The solubility of the metal oxide determines the corrosion resistance of an alloy. As mentioned in the previous section, the molten salt is believed to act as an electrolyte in the electrochemical reactions between the steel surface/ alkali salt. The solubility of metal oxide in the molten salt will directly affect the corrosion rate. According to previous studies, the solubility of metal oxides depends on several factors, such as the presence of other oxides which can cause synergistic oxidation reactions, and the development of solubility gradients in the salt film. The solubility gradient will be described in further detail later in this section.

One significant finding from the early studies of molten salt corrosion is the importance of Na_2O activity within the salt film. The solubility of metal oxides is affected by Na_2O activity and the oxides acid/base reaction in the melted salt film. Oxyanion melts of common alkali salts can exhibit acid/base behavior similar to water. The equilibrium between the acid (SO_3) and base (Na_2O) can be described as sodium sulfate (Na_2SO_4), with the equilibrium constant K at a given temperature. (Rapp, 2002)

$$Na_2SO_4 = Na_2O + SO_3\ (g)$$

$$\log a_{Na_2O} + \log P_{SO_3} = K_{equilibrium\ at\ given\ T}$$

The reaction equations above indicate that any of the molten salt corrosion reactions are electrochemical to their nature and controlled by the sodium (Na_2) activity.

Most metal oxides can have either a basic or acidic reaction depending on the Na_2O activity; those oxides are called amphoteric. (Rapp, 2002) The acid-base character in the salt film is shifted by the salt/alloy reaction, affecting the fluxing of the protective film.

The acidic reaction is typically given as:

$$M_X O_Y = XM^{Y+} + YO^{2-} \text{ where M = metal, O = oxygen}$$

And the basic reaction is typically written as:

$$M_X O_Y + ZO^{2-} = XMO_A^{p-}$$

The evaluation of Na_2O concentration in a given sodium-based salt is called the basicity of a solution and can be measured electrochemically. (Jose et al., 1985) Equilibrium conditions will change as the activity of Na_2O increases or decreases, and more or less of the oxide will react. The solubility will vary within the salt film, thus creating solubility gradients. The solubility gradients can be positive or negative. Depending on the concentration of conjugate acid/base in the melt, oxide solubility either increase (positive gradient) or decrease (negative gradient) away from oxide surface. The increased solubility will allow the oxide ions to remain in the solution and the solution reaches equilibrium, and the corrosion rate slows down. A positive solubility gradient is desired to decrease the corrosion rate.

Whereas a negative solubility gradient suggests that the solubility decreases outwards from the steel surface, subsequently causing the ions to precipitate out of the solution. The negative solubility gradient leads to an out-of-control reaction and an accelerated corrosion rate; therefore, this solubility gradient should be avoided. (Rapp, 1989)

The salt film condition is a significant parameter to consider when investigating metal oxidation. It is most likely that a variation in basicity in the molten salt exists. The solubility and diffusion effects are essential to understand the complex corrosion reactions that occur on the steel surface.

Selection of boiler material

The selection of an appropriate superheater tube material is important to slow down the corrosion process, to ensure maximum boiler availability and performance. The atmosphere to which the metal material is exposed (such as surrounding temperature, flue gas, and deposit composition) is one of the determining factors of material selection. Another major factor is the material price since the required length of superheater tubing for one plant is measured in kilometer length. Enestam noted that, depending on which steel material is chosen, the price varies significantly; therefore, the boiler material selection is very much an economic matter of concern. (Enestam, 2011)

The combustion process environment requires a broad range of properties from the material. The predominant mechanical and physical properties that are required from the superheater materials are ductility, weldability, creep rupture strength, corrosion resistance, and yield strength. Therefore, boiler tube materials range from the cheapest carbon steel to low-alloy steels to high-alloy steels to the most expensive stainless steel/austenitic steels. (Bankiewicz, 2012b)

Although present-day steels can be alloyed with numerous elements, three elements directly impact corrosion resistance: chromium, nickel, and molybdenum. The alloying elements are added to the steel to improve mechanical properties and resistance to corrosion and oxidation.

The main factor that influences the corrosion resistance of an alloy is the ability to form a protective chromium-rich oxide scale on the surface. The more chromium the alloy consists of, the more chromium-rich is the oxide scale that forms. The protective chromium oxide layer is known to form at chromium concentrations greater than 11-12 wt%. The steel surface is self-healing in the air at room temperature, but this requires sufficient oxygen supply and sufficiently high chromium content. If the film does not heal, the corrosion rate is rapid in most environments, allowing oxygen and chlorine to access the metal surface. Main corrosion problems associated with stainless steel are environment-sensitive cracking and crevice and pitting corrosion. Chloride ions are aggressive to the chromium oxide film and intensify the corrosion process. (Trethewey & Chamberlain, 1995)

Low-alloy steels are iron-based alloys with less than 5% of alloying elements and do not contain enough chromium to form the protective chromium-rich oxide layer. The oxide scale of these steels generally consists of Fe_2O_3 and Fe_3O_4 which offer sufficient protection in mildly

corrosive environments at moderate temperatures but not in a corrosive environment at elevated temperatures. In non-corrosive environments and limited temperatures, low-alloy steels are commonly used due to their low price. While at higher temperatures and in more corrosive environments, other steel grades and coatings are used. (Kofstad, 1988) These are iron-based steels that contain less than 5% of alloying elements, including chromium, nickel, and molybdenum. In this study, the ferritic 10CrMo9-10 steel represents this category. (Kofstad, 1988)

Pure iron exists in a body-centered cubic (BCC) structure, at a temperature below 910 °C while above 1400 °C, and in the intermediate range, it has a face-centered cubic (FCC) structure. Alloying elements are dissolved in the iron in both structures. The solution in BCC iron is called ferrite, while the solution in FCC iron is called austenite. Chromium and molybdenum are two examples of ferrite stabilizers. (Talbot & Talbot, 2007)

Iron-based alloys with chromium content typically above 13% and 0–22% nickel are referred to as stainless steels. The stainless steel can either have a ferritic structure (body-centered cubic structure, BCC) or an austenitic structure (face-centered cubic structure, FCC). (Bhadeshia, H. K. D. H. & Honeycombe, 2006) The austenitic structure is only stable at higher temperatures; however, the addition of nickel stabilizes the structure even at lower temperatures. The austenitic stainless steels usually contain more than 16 wt-% chromium and sufficient nickel to stabilize the structure (Trethewey & Chamberlain, 1995). The nickel price is high, so the relative cost of austenitic stainless steel can be as much as three times higher than the low-alloy ferritic steel. The Sanicro 28 austenitic stainless steel studied in this work represents this category of steel.

Nickel can also be used as the base metal of an alloy to improve corrosion resistance at harsh conditions and high temperatures. Despite its superior corrosion properties, nickel-based steels are only used at the most critical parts of the boiler due to their high price. For nickel to retain a fully austenitic structure chromium content is important. The balance between chromium and nickel is therefore economically important due to the high cost of nickel.

Nickel-based alloys are generally used in more corrosive environments. However, despite their superior properties, nickel-based alloys are not generally used in biomass-fired boilers due to their high price. The nickel-based Alloy 625 represents this category of alloys in this work.

Corrosion test method

The experimental part of this work is performed according to the Åbo Akademi standard one-week corrosion test. For the corrosion tests, a synthetic alkali salt is produced to simulate the ash deposit in the actual boiler conditions. The alkali salts, that are used in the corrosion tests are well-characterized salt mixtures with a specific melt behavior and chemical composition. An analysis is performed on the produced salt mixture to check the chemical composition of the salts. Besides the chemical composition, also the melting behavior of the salt mixture is an important parameter to consider in this work. To check the melting behavior of the salts, thermodynamical calculations are conducted based on the chemical composition data obtained from the qualitative analysis.

The following sections give an overview of the ÅA standard corrosion test method, the analyzing techniques used in the process, and the salt characterizing procedure.

ÅA standard corrosion test method

The Åbo Akademi standard corrosion test method consists of a sequence of three steps, first, pre-treatment and furnace exposure, second, the determination of the oxide layer thickness along the metal surface with SEM/EDX analysis, and third, analysis of the corrosion layer based on SEM images, elemental maps, corrosion layer distributions further to analyze the corrosion mechanisms at the steel surface.

In the pre-treatment step, steel coupons of approximately 20x20 mm and thickness of 5 mm, are polished and washed, whereafter a thermally stable paste is applied at the edges of the steel specimen to keep the salt in place. The steel coupons are then pre-oxidized in a furnace at 200 °C for 24 h. After the pre-oxidizing step, a synthetic ash/ salt is applied onto the steel surface. The steel specimens are put into a horizontal furnace for a week's corrosion experiment. The corrosion furnace and sample holder used during the corrosion experiments are presented in Figure 1. The temperature inside the furnace is measured with thermocouples installed between adjacent samples and at both ends of the sample holder to control the temperature during the experiments.

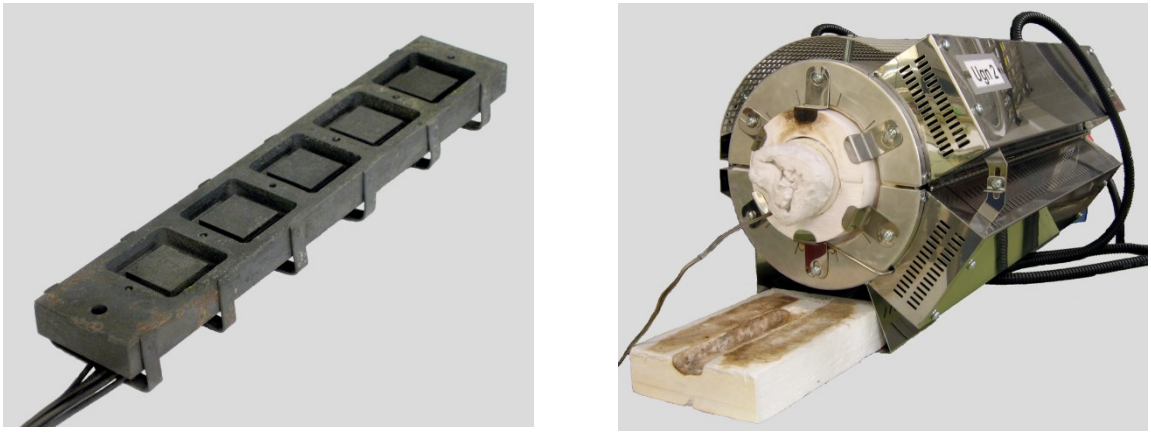

Figure 6. a.) sample holder for exposure up to 5 samples at a time, b.) Horizontal tube furnace. Photographs are courtesy of Linus Silvander.

After the furnace exposure, steel samples are cast in epoxy and cut in half to reveal the cross-section area preparing the samples for the second step in the corrosion test method.

In the second sequence, the corrosion samples are analyzed by means of Scanning Electron Microscope/Energy Dispersive X-ray (SEM/EDX) using backscatter electron mode to identify various chemical elements in the sample. The X-ray images show the elemental composition of corrosion products at the sample. The working principle of the scanning electron microscope is described later in the section analyzing techniques.

A specific area chosen from the corrosion layer is analyzed by using the SEM backscatter electron mode to identify the distribution of the oxide layer thickness. The SEM images are combined into one panoramic image and then colored with contrast colors. The coloring treatment stages of a typical SEM panoramic picture are presented in Figure 4.

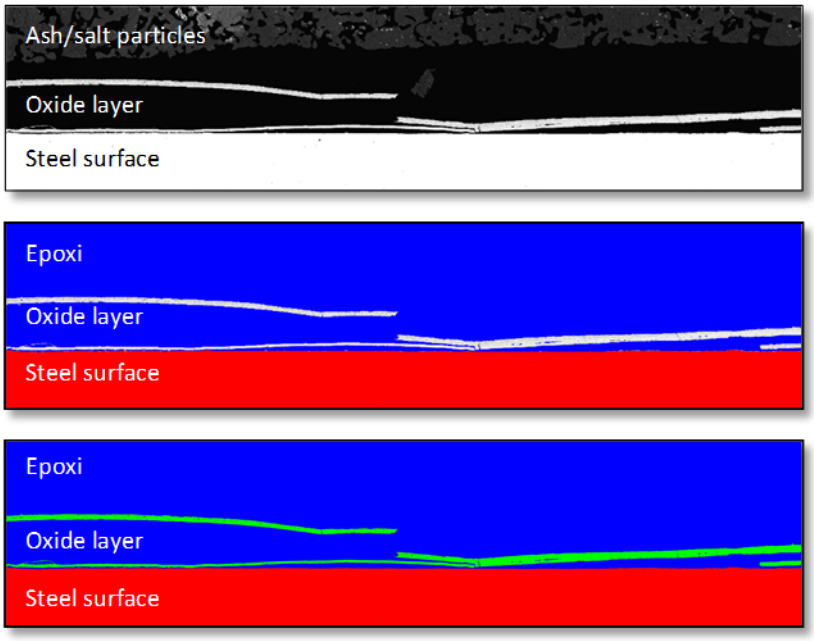

Figure 7. A schematic view of the coloring stages of SEM pictures to determine oxide layer thickness.

After the panoramic image has been colored to green (oxide layer), blue (epoxy), and red (steel surface), the corrosion layer thickness is determined for each vertical line of pixels and is then recalculated into µm. Corrosion is defined as the thickness of the oxide layer above the steel surface and some possible degradation of the steel under the oxide layer. The corrosion is expressed as mean corrosion layer thickness across the analyzed steel surface. From the thickness corrosion analysis also thickness distribution curves are obtained.

The third step in the sequence includes the selection of an area representing the average corrosion layer. From this area, elemental maps of the oxide scale and the steel surface are produced to analyze the elements in the oxide scale. Figure 3 presents an example of some of the elemental maps that are considered when analyzing the corrosion products. The light area in the elemental maps consists of higher concentration atoms of the element given in the upper left corner of the image.

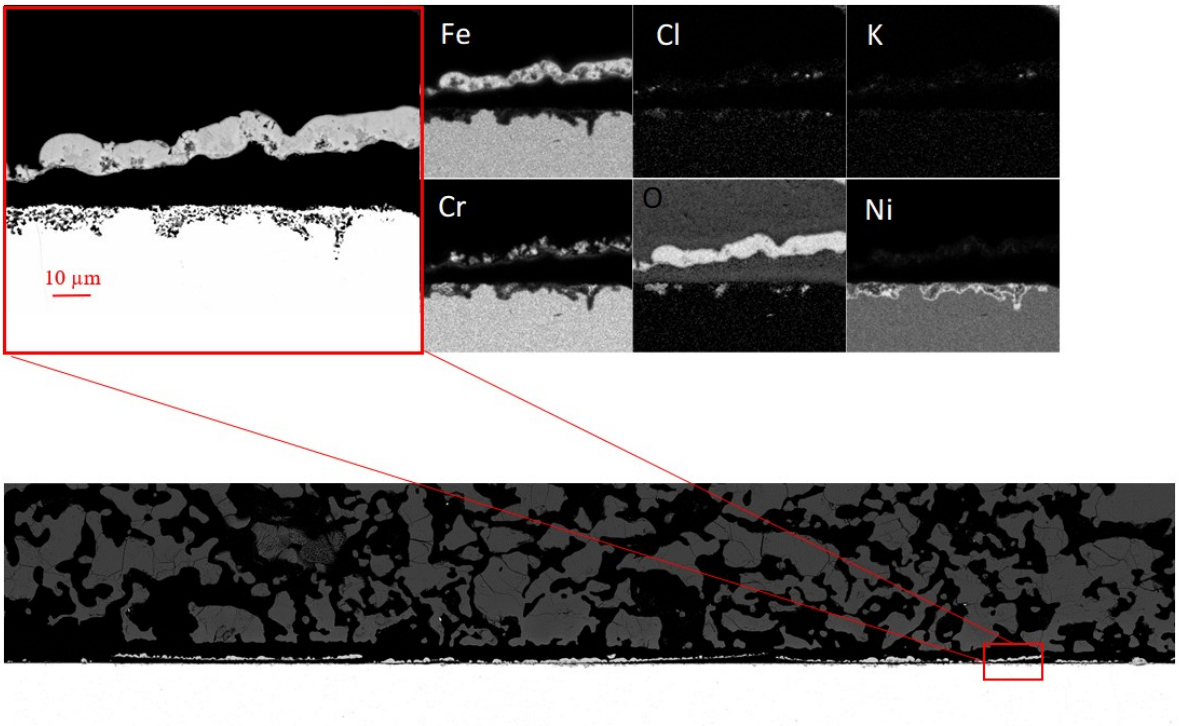

Figure 8. SEM image and the corresponding elemental maps from the area inside the red box.

Salt characterization

A well-characterized alkali salt, simulating an ash deposit in the boiler, is produced and applied to the steel surface before the corrosion tests. To obtain well-characterized salts, the chemical composition of the salts is analyzed. In this work, the total chemical composition was analyzed with scanning electron microscopy, and additionally, the chlorine concentration of the salt was also analyzed with ion chromatography. Based on the chemical composition from the SEM analysis, melting curves and T_0 of the synthetic salt were produced based on thermodynamic calculations with the software Factsage 7.3 (Bale et al., 2016) using the FTpulp database. The analyzing techniques are described in further detail in the following section.

Analyzing techniques

Scanning electron microscope/energy dispersive x-ray is used to analyze both the composition of the produced salt and to analyze the components in the corrosion layer from the corrosion experiments. The chlorine concentration of the salts is also analyzed by means of ion chromatography. Lastly, the thermodynamic calculation method used to obtain the melting behavior of the salts is shortly presented.

SEM/EDX

The exposed steels and the salt mixtures were characterized with SEM - LEO Gemini 1530 with a Thermo Scientific UltraDry Silicon Drift Detector manufactured by Leo (2001) and EDX – ThermoNORAN Vantage X-ray analyzing system manufactured by Thermo Scientific (2009). The SEM-EDX is an advanced analytical technique for the chemical characterization of the surface of a sample. The sample surface is scanned with an electron beam gun. The electron beam generates a large number of signals, such as the emission of secondary electrons (SE), backscattered electrons (BSE) from the primary beam, and the creation of element-specific X-rays. Secondary electrons are generated when the inner core electrons of the surface atoms are ionized by the primary beam. Backscatter electrons are generated by the scattering of the primary electron beam by the sample atoms. The impact of the electron beam on the sample produces X-rays that are characteristic of the elements found on the sample. The SE signal is most useful to show topography and morphology, while BSE are used to show differences in the composition of the sample. Backscattered electrons display different elements with different darkness in the image; lighter colors represent a heavier element in the sample. The SEM images used in this work are mainly in a backscattered electron mode. (Goldstein et al., 2018) The oxide layer thickness and the thickness distribution on each specimen were evaluated based on the panorama SEM technique. Additionally, the chemical composition of the salt mixture was analyzed with scanning electron microscopy.

Ion Chromatography

Ion chromatography measures the concentration of ionic species in a water solution, and in this work, it was used to analyze the concentration of chlorine in the salt mixtures. The method separates ions and polar molecules based on their interaction with a resin (stationary phase). The solution passes through a pressurized chromatographic column, and the ion is adsorbed on the column's constituents. The ions are separated from the column by running an eluent, ion extraction liquid through the adsorbed column. The time it takes for the ionic species to move through the column varies depending on their interaction with the column. Ions with a weaker affinity for the column will move through the column faster, while ions with higher affinity will move through the column more slowly. The variation of affinity is due to differences in ion charge and size. Ions are measured with an electrical conductivity detector as they exit the column. This detector produces a chromatogram that plots conductivity vs. time. The

chromatogram consists of various peaks that represent different species; the area under these peaks correlates with the concentration of the species. (Gjerde et al., 1987)

Thermodynamic calculation method

Thermodynamic equilibrium calculations are used to investigate the melting behavior of the simulated ash deposit. Thermodynamic calculations are performed based on a thermodynamic multi-component, multi-phase equilibrium calculations with the software Factsage 7.3 using FTpulp database (Bale et al., 2016). The input data for the calculation, are the experimental data from SEM analysis of the salts. These calculations are made to check the melting behavior of the salts, such as T_0 and the amount of melt formed at T_0. Figure 4 presents one of the melting curves that are produced based on the thermodynamic calculations with the software Factsage 7.3. In the graph, T_0 is read out from the intersection of the curve and x-axis.

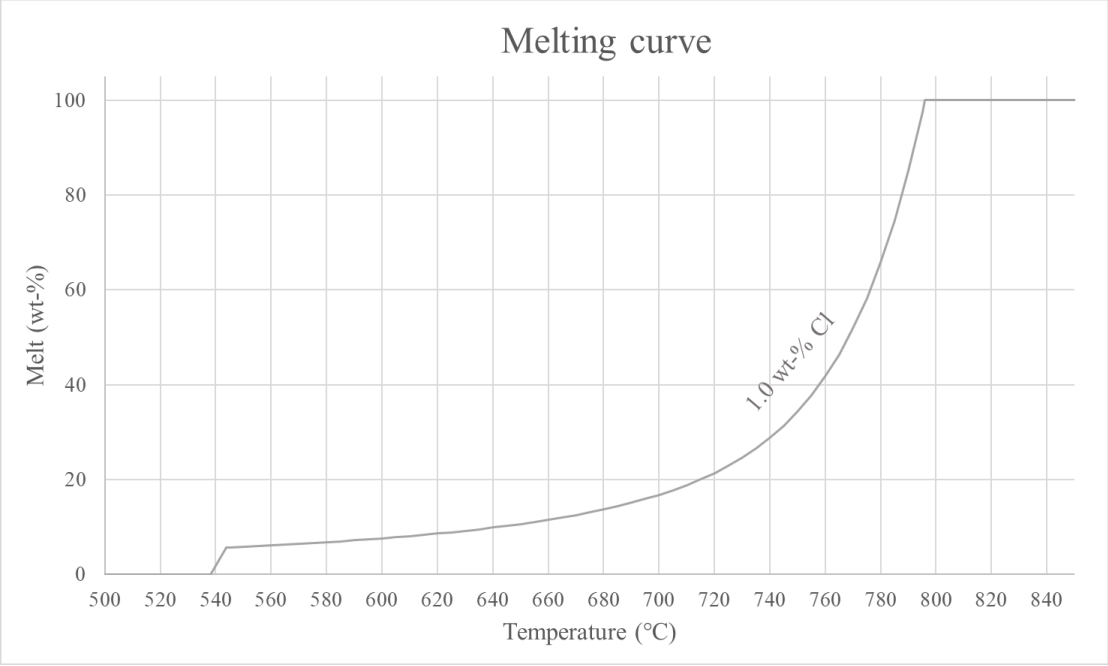

Figure 9. Melting curve of the salt mixture with 1.0 wt-% chlorine that is produced based on the thermodynamic calculation with the software Factsage 7.3.

Experimental

The experimental part of this work consists of a laboratory-scale corrosion study with three alloys typically used as heat-transfer materials. The steel materials were exposed to five different tailor-made well-characterized synthetic alkali salt deposits. The experiments were one-week corrosion experiments for each steel-salt combination, both below T_0 at 520 °C and above T_0 at 560 °C, to be able to compare the corrosion resistance both above and below T_0. This resulted in a total of 30 corrosion tests. Additionally, each test was carried out as duplicates; therefore, the total amount of tests was 60 steel coupons.

The test matrix is presented in Table 1. The salt cases are named after the concentration chloride in the salt mixture; for instance: Case 0.25 consists of 0.25 wt-% chloride. The target chemical composition of the salt is presented in more detail in Table 2, where each column presents the composition of one salt case.

Table 3. Experimental matrix for all materials of the study.

	Case 0.25		**Case 0.5**		**Case 1.0**		**Case 2.0**		**Case 10.0**	
	Temperature		Temperature		Temperature		Temperature		Temperature	
Sanicro 28	520	560	520	560	520	560	520	560	520	560
10CrMo	520	560	520	560	520	560	520	560	520	560
Alloy625	520	560	520	560	520	560	520	560	520	560

Table 4. The composition of the tailor-made synthetic alkali salt mixtures used in the corrosion tests. The composition is given in wt-%.

	Case 0.25	**Case 0.5**	**Case 1.0**	**Case 2.0**	**Case 10.0**
Na	31.33	31.34	31.37	31.44	31.96
K	4.95	4.95	4.95	4.96	5.05
SO_4	50.64	50.44	50.02	49.15	42.28
Cl	0.25	0.49	0.97	2.00	9.99
CO_3	12.83	12.78	12.68	12.45	10.71
T_0 (°C)	538	538	538	538	538

Pre-treatment

The test specimens were received in a size of approximately 20x20 mm and a thickness of 5 mm. Before the experiments, all the steels were polished with water and 360 grit sandpaper and then with ethanol and 1000 sandpaper. The polished steels were then washed in an ultrasound bath in ethanol. A thermally stable paste was applied around the edges of the steel to prevent the molten salt from flowing off of the surface. Before the corrosion tests started, the polished steel samples were pre-oxidized in a furnace at 200 °C for 24 hours. The pre-determined synthetic salt deposit was placed on each coupon before exposure (~ 0.25 g/specimen). The salt powder was lightly pressed and spread out over the steel surface with a glass rod to ensure better contact between salt and material surface.

Furnace exposure

The high-temperature corrosion tests were performed in a horizontal silica tube furnace at two temperatures, 560 °C, and 520 °C. The exposure time was 168 h ± 2 h (7 days) in an ambient atmosphere. The horizontal tube furnaces were presented in chapter 1.1, where the ÅA standard corrosion test method was described.

After the furnace exposure, the samples were allowed to cool down to room temperature outside the furnace. The samples were covered with a layer of epoxy resin to prevent further oxidation and to fix the corrosion products to the steel surface. The samples were put into a vacuum to remove air pockets and then dried until the next day. The following day, the samples were put into a mold and cast into epoxy, and dried. The epoxy piece was cut in the middle with oil to expose the cross-section of the sample. The sample was further cleaned with petroleum ether in an ultrasound bath to remove excess oil. An epoxy layer was further added to the cross-section surface and put into a vacuum to fill out the cavities in the sample. The cross-section was polished in kerosene, which was used as a polishing lubricant to avoid dissolution of the chlorine-containing compounds. The samples were first polished manually with 360-grain size sandpaper and then polished with a machine using 500, 1200, 2000, and 3 µm (besides kerosene, a diamond paste was added to 3 µm). The samples were washed with petroleum ether in an ultrasound bath and put into a vacuum to extract the oil from the sample.

Method to analyze corrosion data

The corrosion results of this work are presented as SEM images, mean oxide layer thickness, maximum oxide layer thickness, 90^{th} percentile value of corrosion thickness, oxide layer thickness distribution curves, and elemental maps of the oxide composition. The mean measured oxide layer thickness gives a general picture of how the corrosion had proceeded over the whole specimen, not only a randomly chosen point. From the corrosion layer thickness, an estimation of the steel performance can be evaluated with the help of some pre-determined corrosion ranges that are based on practical experience in an actual boiler. Some variation in corrosion result might occur in case someone else was to repeat the experiments; therefore, further experiments are recommended to check reproducibility and to observe some typically repeated corrosion behavior. Mean oxide layer distribution curves were used to suggest the type of corrosion attack. The shape of the distribution curve can be used to estimate the type of corrosion: A narrow distribution suggests that homogeneous corrosion occurred over the whole surface, whereas a broad and possibly tailing distribution would imply that more heterogeneous corrosion took place.

Salt preparation and analysis

In this section, a detailed description of the salt preparation and characterization will be presented.

For the corrosion tests of this work, synthetic alkali salts with tailor-made melting characteristics were produced using sodium sulfate Na_2SO_4, potassium sulfate K_2SO_4, sodium chloride NaCl, sodium carbonate $NaCO_3$ as starting material. The synthetic alkali salts containing sulfates and chlorides of sodium, potassium was composed in such a way that their first melting temperature (T_0) is the same for all cases, but the amount of molten phase at T_0 varied for each salt mixture. The chemical compositions of the final salts were checked to ensure that it was close to the planned compositions. Based on the chemical composition of the final salt, melting curves and T_0 of the synthetic salt was calculated based on thermodynamic calculations with the software Factsage 7.3 (Bale et al., 2016) using the FTpulp database.

The tailor-made synthetic alkali salts were prepared by weighing and mixing the starting material. Before weighing, starting material was dried to remove moisture and water from hydrates. After the components were mixed, they were heated to 930 °C for about 20 minutes

and then cooled down to room temperature. The cooled salt was crushed and sieved to a grain size between 53 and 250 µm. The purpose of the pre-treatment of the alkali salt mixtures was to homogenize the salt mixture to imitate the recovery boiler process, where the flue gas dust goes through a melting stage.

The chemical composition of the produced salts was analyzed by means of Scanning Electron Microscopy (SEM) to ensure that the final salt composition is close to the target. Before the SEM analysis, the salt powder was pressed into pills, and surface analysis was performed. Table 2 presents the results from the SEM analysis. The SEM analysis results showed that the chloride content was higher than the target composition in the plan; therefore, further analysis was conducted with Ion Chromatography. The wet chemical analysis of the salt mixture is a more quantitative method to analyze the salt mixture. The salt mixtures were dissolved in elga water so that the chlorine concentrations were approximately 10 ppm and 5 ppm. The result from the IC analyses is presented in Table 4 and Table 5. The IC analysis results were close to the target composition, which confirmed that the planned composition was achieved.

Table 5. Elemental composition of the salt cases based on the SEM analysis.

Element	Case 0.25	Case 0.5	Case 1.0	Case 2.0	Case 10.0
Na	32.02	31.85	32.21	32.11	33.03
K	4.06	4.21	4.36	4.21	4.14
SO_4	50.50	50.73	47.61	48.53	39.68
Cl	0.42	0.69	1.14	2.19	10.79
CO_3	13.00	12.52	14.67	12.97	12.35

Table 6. Elemental composition of the salt cases based on IC analysis with 10 ppm concentration chlorine.

Element	Case 0.25	Case 0.5	Case 1.0	Case 2.0	Case 10.0
Na	-	-	-	-	-
K	-	-	-	-	-
SO_4	-	-	-	-	-
Cl	0.26	0.51	1.02	2.25	11.48
CO_3	-	-	-	-	-

Table 7. Elemental composition of the salt cases based on IC analysis with 5 ppm concentration chlorine.

Element	Case 0.25	Case 0.5	Case 1.0	Case 2.0	Case 10.0
Na	-	-	-	-	-
K	-	-	-	-	-
SO_4	-	-	-	-	-
Cl	-	-	-	1.8	9.3
CO_3	-	-	-	-	-

In the following section, the melting behavior of the produced salt mixtures will be presented.

Melting behavior of salts

Thermodynamic equilibrium calculations (using Factsage 7.3) were made based on the actual salt compositions obtained from the SEM analysis. Based on the thermodynamic equilibrium calculations, melting curves and melt compositions of the salt mixtures were produced. The results from the SEM analysis were used as input data for the thermodynamic calculations.

Figure 3 presents the melting behavior of the salt cases. The first melting temperature calculated from the actual salt cases is not the same for all cases, which is seen as the melt curves do not intersect with the x-axis at the same point. This is due to small differences in the actual composition of the salt mixtures compared to the target compositions. Nevertheless, T_0 for the different cases does not deviate much from the target. The melt curve for the salt case with 10.0 wt-% chlorine shows a steep increase at 560 °C, which means that the melt fraction is sensitive to temperature changes. As for the other salt mixtures, the curves have reached a plateau before 560 °C.

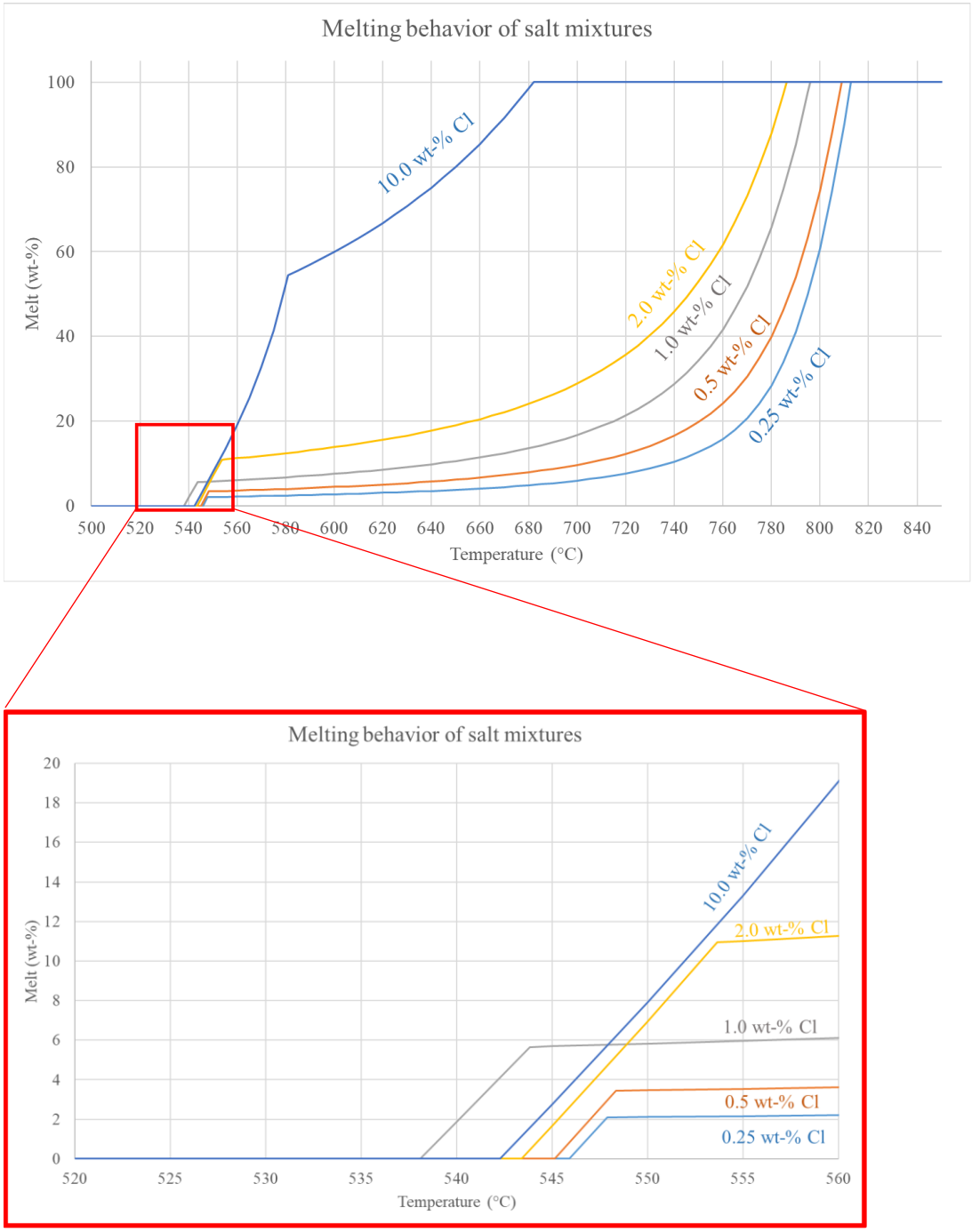

Figure 10. The calculated melting behavior of the salt mixtures presented as the amount of molten phase in the salt mixture as a function of temperature. The amount of melt is expressed as wt-% of the total mass of the condensed phase. Top: whole melt curves bottom: a focused image of the interesting area in this work.

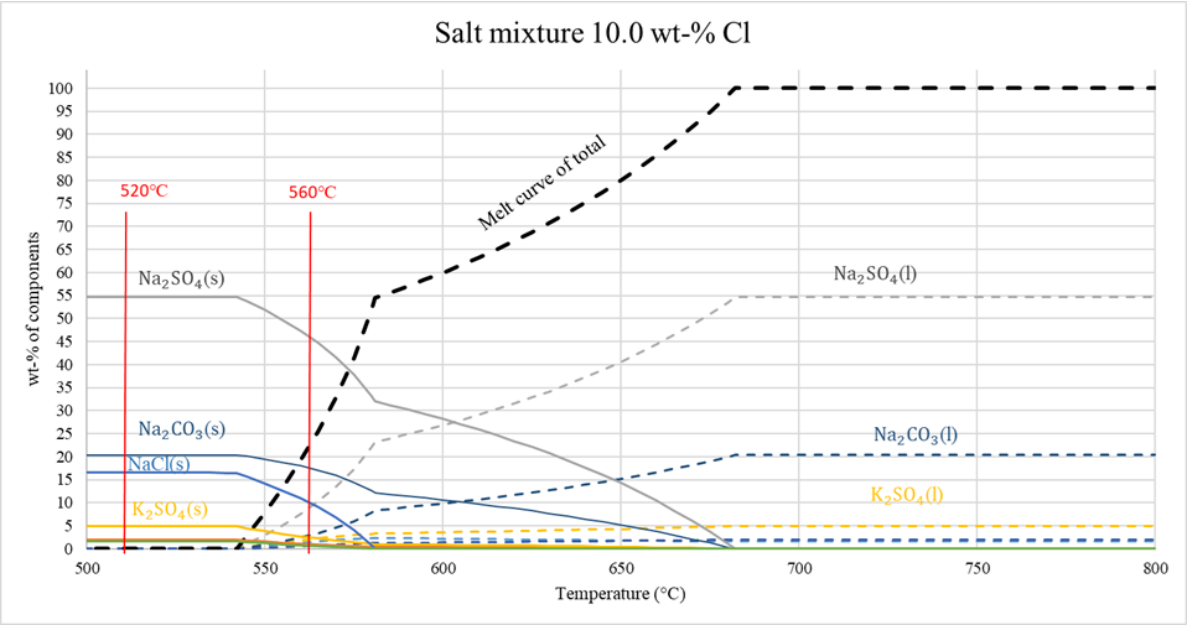

Figure 11. Presentation of the components present in the different phases at different temperatures.

The melt composition of the alkali salts is displayed in a bar diagram as the composition of the molten phase at 560 °C (Figure 4). The amount of solid phase of a specific component can be read from the figure.

The bar diagram below presents the composition of the molten phase for all salt mixtures tested in this work. The target melt composition is also included in the diagram. The melt composition is almost the same for all cases, and they correspond to the target composition.

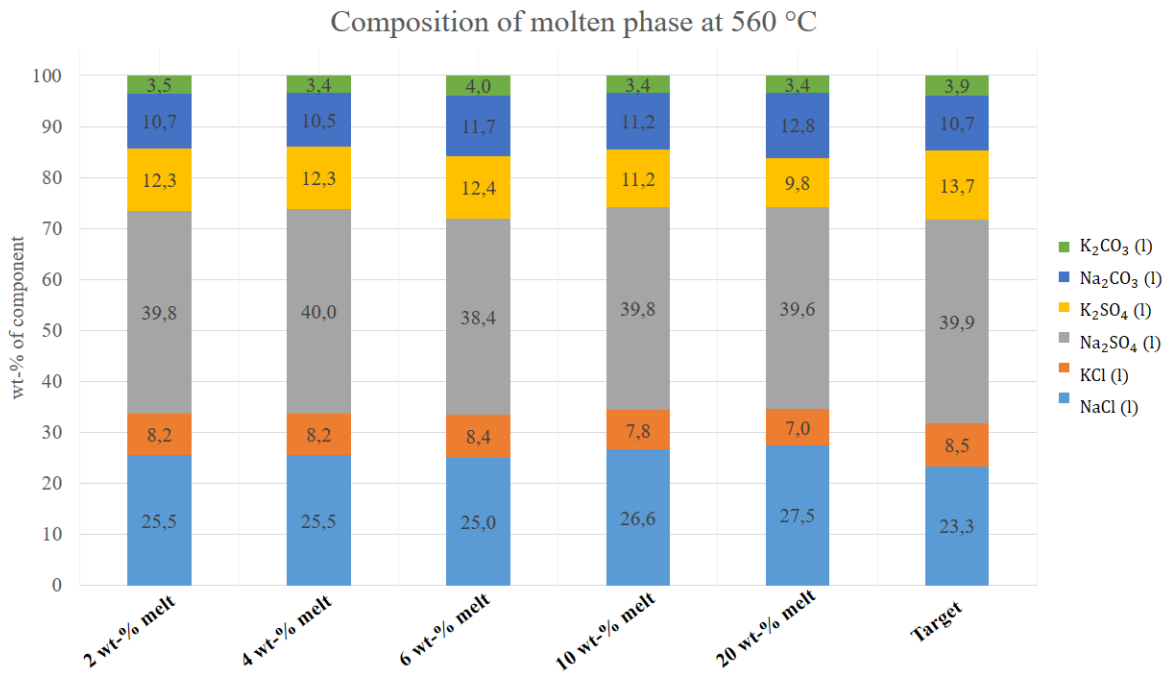

Figure 12. Composition of molten phase for the salt cases and the target melt composition.

Tested steels

The chemical composition of the steels tested in this work is presented in Table 3. Two of the steel materials are typical Kraft recovery boiler superheater steel materials, low-alloy steel, 10CrMo9-10, and the austenitic stainless steel, Sanicro 28. The third steel that was chosen for the corrosion experiments was the nickel-based alloy, Alloy 625. The quality and corrosion resistance of the alloys vary due to their alloying elements. The ferritic 10CrMo9-10 low-alloy steel consists mainly of iron and low amount alloying elements, and as a consequence, this material is not protected by a chromium-rich oxide. Instead, low-alloyed steels rely on iron oxides as protection against corrosion. Sanicro 28 contains considerably higher concentrations of Cr and Ni than 10CrMo9-10 and therefore exhibits a better corrosion resistance. Alloy 625 consists of significantly low iron content and high chromium and nickel content.

Table 8. Chemical composition of alloys, given in percent. The chemical compositions of the alloys are given as nominal chemical composition or limiting chemical composition. (Suomen standardisoimisliitto, 2008) (*Special material corporation.* 2013) (*Sandvik Sanicro 28.*)

Steel	Cr	C	Ni	Mn	Mo	Si	Definition
10CrMo9-10	2.00-2.50	0.08-0.14	≤ 0.30	0.30-0.70	0.90-1.10	≤ 0.50	
Sanicro 28	27.0	≤0.02	31.0	≤ 2.0	3.5	≤ 0.7	Nominal composition
Alloy 625	20.0-23.0	0.10 max	58 min	0.5 max	8.0-10.0	0.5 max	Limiting composition

Results and discussion

Summary of corrosion results

Table 4 summarizes the oxide layer thickness values for the 30 steel-salt cases. The table gives the mean oxide layer thickness values, expressed as µm, for the three steel sets covered with the five salt cases. The two first columns to the left in the table identify the steel used in the test and the temperature of the test run. The different salt cases are as columns in the table.

As can be seen from the table, the low-alloy steel corrodes in all cases, while the nickel-based alloy, Alloy 625, resists corrosion the best. However, all steels showed some corrosion above T_0, with the highest melt fraction tested in this work.

A corrosion color indication is introduced as a tool to highlight the corrosion behavior of the steel tested in this work. In a previous corrosion study at Åbo Adademi by Bankiewicz, certain ranges of the corrosion layer thickness were introduced. (Bankiewicz, 2012a) The color indication in this work consists of the colors of a traffic light, and the suggested ranges are based on the experience that 20 µm/ week in laboratory experiments corresponds to the threshold for unacceptable corrosion in actual boiler conditions. A summary table of the corrosion results with the color indication is presented in Table 4, and the suggested corrosion thickness ranges here are:

Green: (<10 µm/week) Corrosion is detectable but not significant

Yellow: (10-20 µm/week) Low corrosion

Red: (>20 µm/week) Significant corrosion

Table 9. Summary of corrosion results.

		Case 0.25	Case 0.5	Case 1.0	Case 2.0	Case 10.0
Steels	Temperature (°C)	Oxide layer (µm)	Oxide layer (µm)	Oxide layer (µm)	Oxide layer (µm)	Oxide layer (µm)
10CrMo	560	48	55	77	143	146
	520	58	54	38	69	52
Sanicro28	560	5	7	12	10	23
	520	3	2	4	2	2
Alloy625	560	3	2	3	0+	4
	520	0+	2	0+	1	1

In the following sections, the corrosion results are presented in further detail, steel by steel.

10CrMo9-10

The corrosion results for 10CrMo9-10 are summarized in Figure 5. Additionally, a red line was added to the graph to indicate the limit for significant corrosion layer thickness. As can be seen from the graph for the low-alloy steel 10CrMo9-10, significant corrosion was observed for all melt fractions tested. Significant corrosion was also detected below T_0 when no molten phase was present in the deposit. A considerable increase in corrosion layer thickness was observed when the molten phase increased from 6-10 wt -% melt. No significant change in oxide layer thickness was observed below T_0, despite the increased chlorine content in the salt.

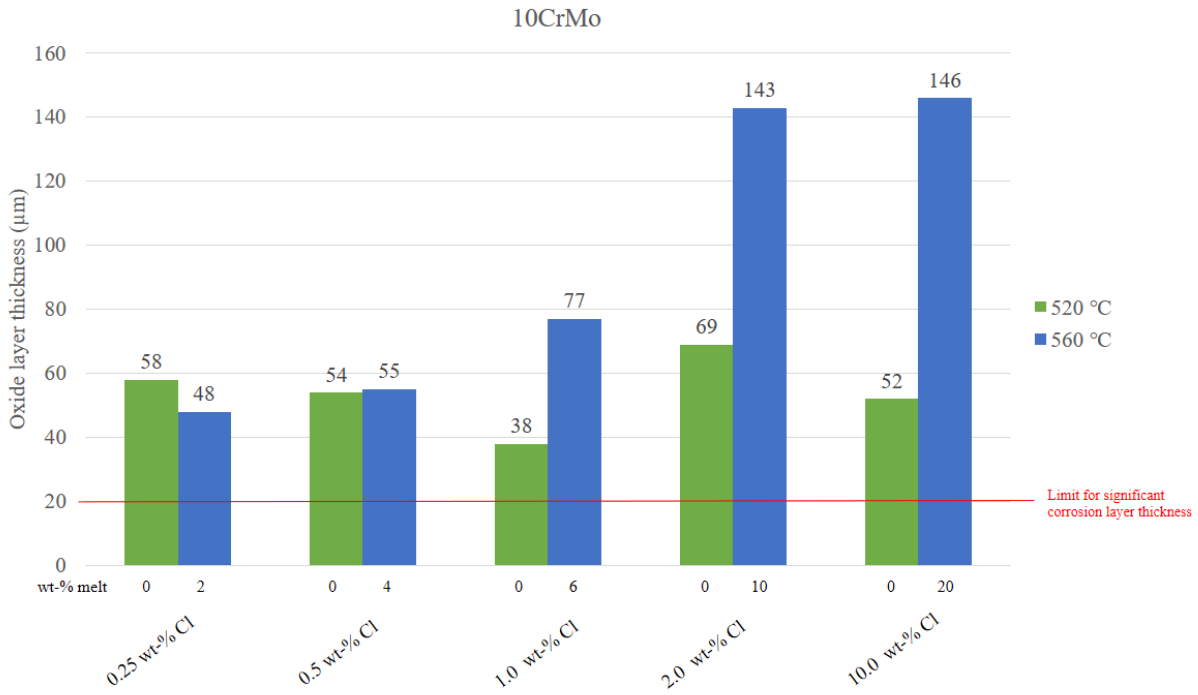

Figure 13. Summary of the mean oxide layer thickness values for the tests with 10CrMo9-10. Exposure time: 168 h, atmosphere: air, temperatures: 560 and 520 °C. The x-axis identifies the wt-% Cl in the salt deposit and the corresponding wt-% melt.

Elemental distribution in the oxide layer

The compositions of the corrosion layers were analyzed by X-ray mapping, and the results are shown in Figure 6. The oxide layer formed on 10CrMo9-10 steel was typically developed in the form of separated, thin layers of corrosion products. This layered form of oxide scale is typically observed on low-alloy Fe-based steels since iron chloride converts into oxide at higher oxygen partial pressure than chromium oxide. (Zahs et al., 2000). The corrosion products identified by the X-ray mapping revealed that iron oxide was located at the outer part of the oxide scale, and chromium oxide was mainly located towards the steel surface. A compact oxide layer was formed on some of the samples; however, no specific pattern of what would cause that was observed. In the image above, clear layers of melt elements are detected just below the iron oxide scale, forming layers that might consist of alkali chromate, salt elements, and iron oxide at the outer part.

10CrMo9-10, 560°C, 1.0 wt-% Cl, ~ 6 wt-% melt

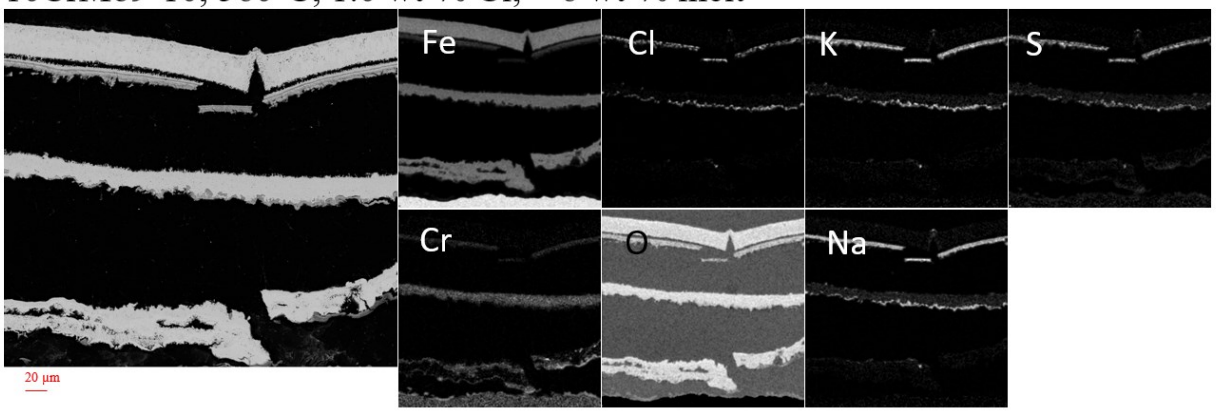

10CrMo9-10, 520 °C, 1.0 wt-% Cl

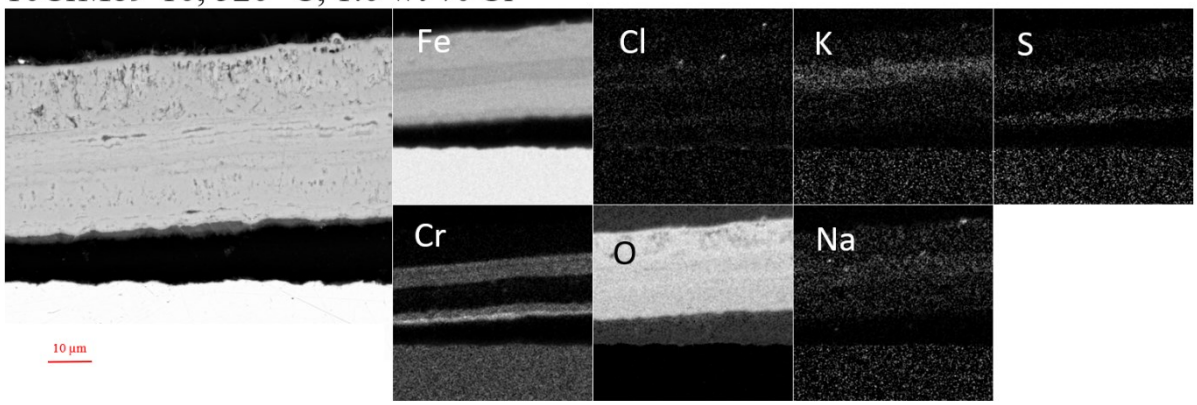

Sanicro 28

The corrosion results for Sanicro 28 are summarized in Figure 10. A red line was also added to this graph to indicate the limit for significant corrosion layer thickness. It is important to note that the scale for this graph is different than the graph of 10CrMo9-10. As can be seen from the graph, Sanicro 28 withstood corrosion significantly better than 10CrMo9-10, but also this steel showed increased corrosion as melt fraction increased in the deposit. According to the results, no significant corrosion was detected for Sanicro 28 up to 4 wt-% melt. Low corrosion was detected for 6 wt-% and 10 wt-% melt. Further, significant corrosion was observed at the highest tested melt fraction, 20 wt-% melt.

In Figure 10, a summary of the SEM images of Sanicro 28 is shown. Each column displays the SEM image from the corrosion tests above and below T_0 (560 and 520 °C) for each steel-salt combination. As can be seen from the SEM images in Figure 8, samples exposed below T_0 all showed a thin corrosion thickness and similar corrosion behavior, while the ones above T_0 showed an increase in the corrosion layer thickness.

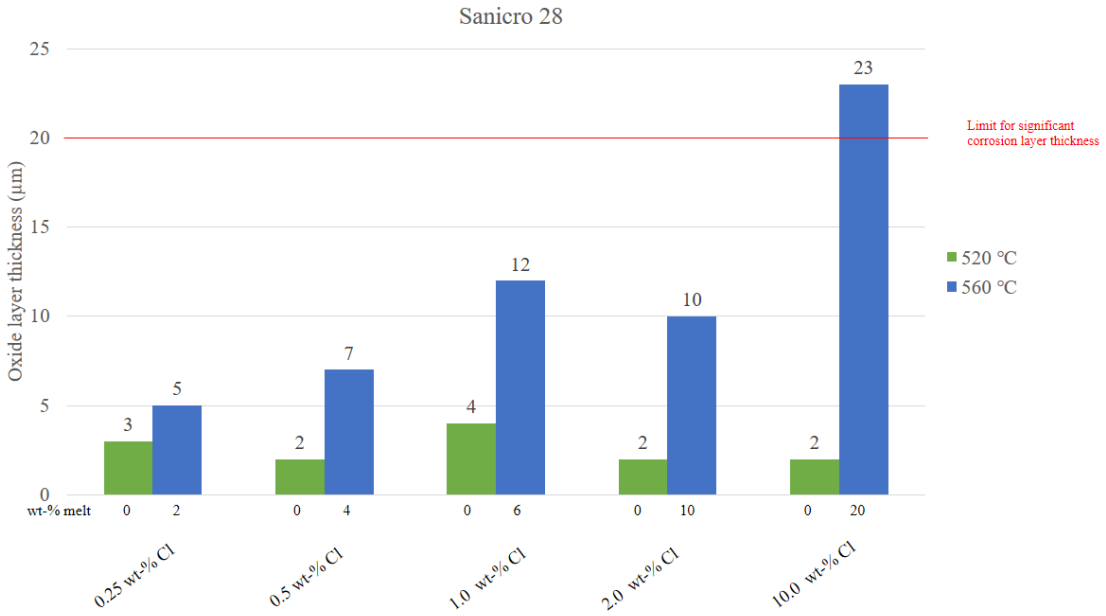

Figure 14. Summary of the mean oxide layer thickness values for the tests with Sanicro 28. Exposure time: 168 h, atmosphere: air, heat treatment temperatures: 560 and 520 °C. The x-axis identifies the wt-% Cl in the salt deposit and the corresponding wt-% melt.

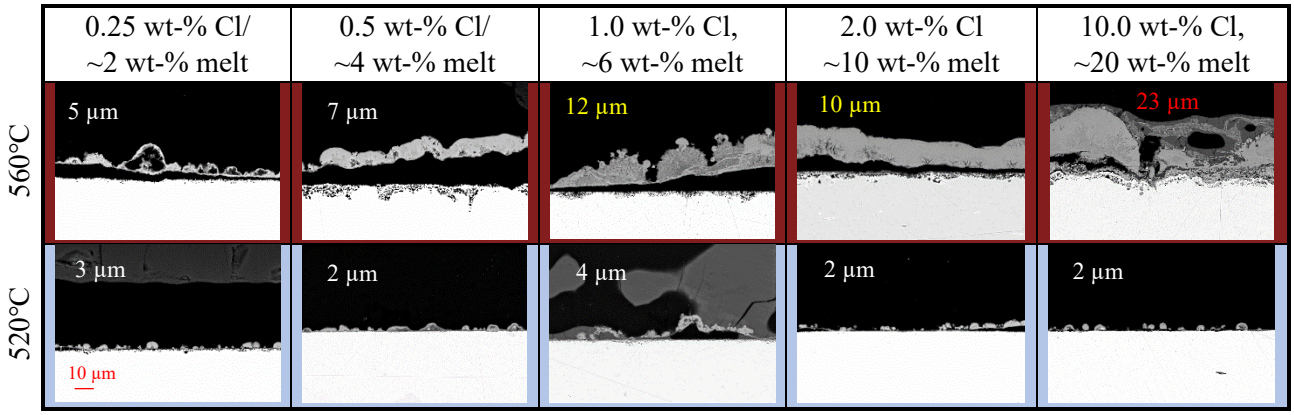

Figure 15. SEM image of the steel surface from all corrosion experiments of Sanicro 28. All images in the table have the same scale.

Elemental distribution in the oxide layer

The composition of the corrosion layers of Sanicro 28 is presented in Figures 12-16. Sanicro 28 showed some similar corrosion patterns as 10CrMo9-10, but to a much lesser extent at the lower melt fractions. Iron oxide had formed at the outer part of the oxide layer and chromium oxide towards the steel surface. As previously mentioned, due to the difference in

thermodynamic stability of metal chlorides, the iron oxide formed further away from the steel surface because iron chloride evaporates and diffuses further away from the steel surface before it oxidizes.

Figures 12-15 show the corrosion results of the tests at 560 °C (i.e., above T_0). A nickel-rich region is observed at the interface of the oxide and the bulk steel, most likely a porous nickel skeleton after the iron and chromium are depleted at the alloy. The same iron and chromium depletion has been observed in previous studies (Nielsen et al., 2000) (Pettersson, C. et al., 2008). The nickel-rich region extends deeper into the metal for the cases with a higher melt fraction in the deposit, which is as expected since more chromium and iron have depleted the bulk steel. Potassium chromates have likely formed and are present in the oxide scale, which supports the theory that corrosion is initiated with potassium reacting with chromium oxide. The formation of potassium chromate depletes the scale in chromium and leads to the formation of a non-protective porous iron-rich oxide scale. The iron-rich oxide is unable to protect the steel at high temperatures. (Pettersson 2006)

Some Cl and K were observed at the Fe depleted zone, Figure 12. Otherwise, no significant amounts of chlorine could be detected at the steel surface for the other tests. In the study by Skifvars et al. at similar conditions, more chlorine was detected at the steel surface compared to the result in this work.

At the highest tested melt fraction, a mixture of corrosion products and salt melt is formed above the surface of Sanciro 28, Figure 15. Chromium oxide is surrounded by iron oxide, which is surrounded by salt components. While only a small oxide layer was formed when the same steel/salt combination was exposed to furnace condition below T_0, see Figure 16.

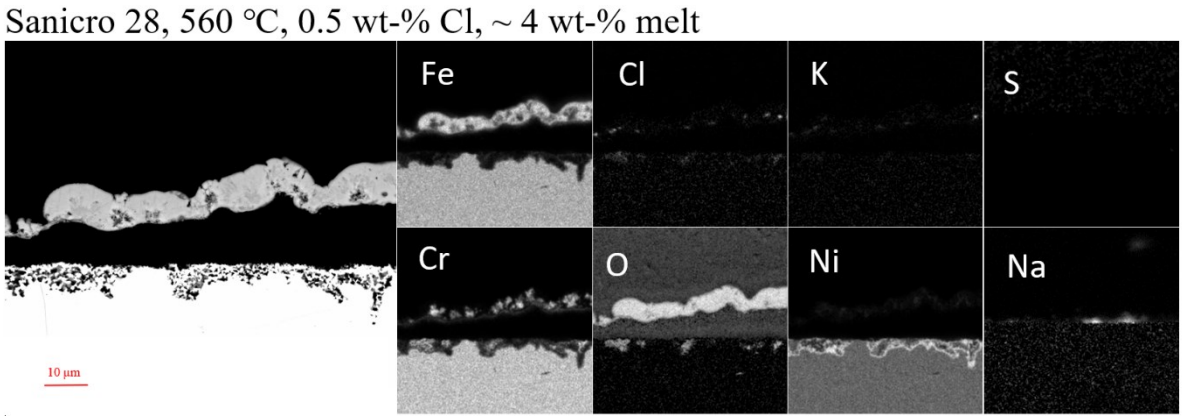

Figure 16. SEM/EDX element X-ray maps of the Sanicro 28 steel coupon cross-section area. The heat treatment temperature 560 °C deposited with salt case 0.5 wt-% Cl, ~4 wt-% melt.

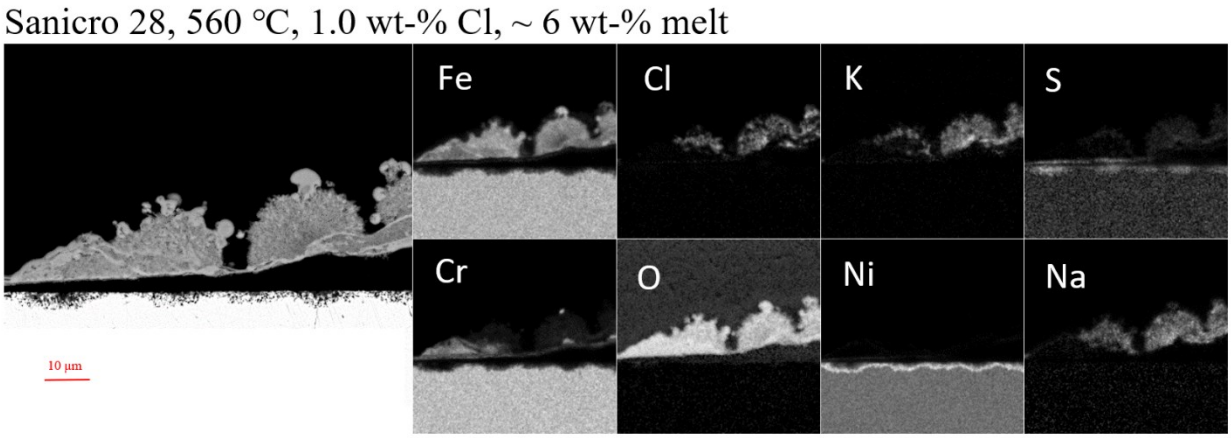

Figure 17. SEM/EDX element X-ray maps of the Sanicro 28 steel coupon cross-section area. The heat treatment temperature 560 °C deposited with salt case 1.0 wt-% Cl, ~6 wt-% melt

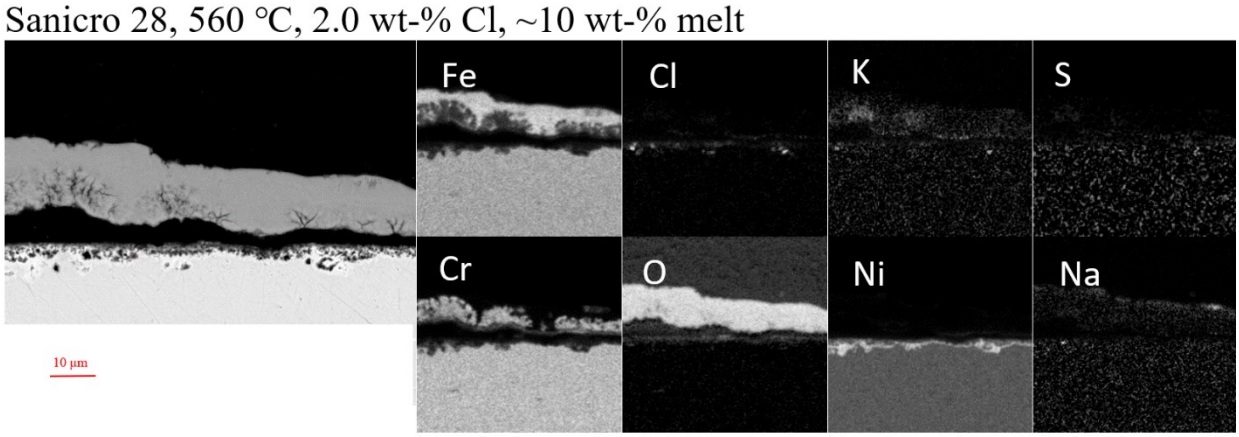

Figure 18. SEM/EDX element X-ray maps of the Sanicro 28 steel coupon cross-section area. The heat treatment temperature 560 °C deposited with salt case 2.0 wt-% Cl, ~10 wt-% melt

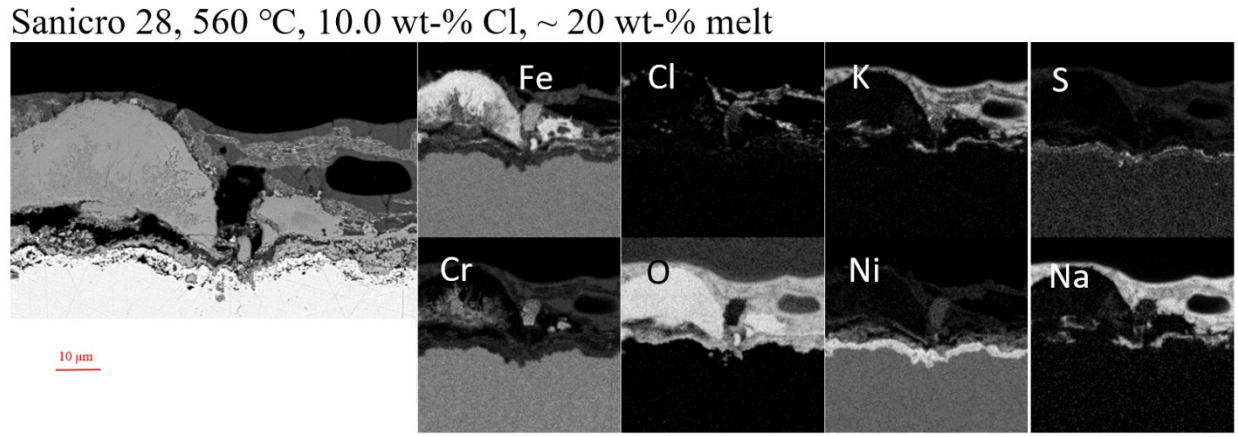

Figure 19. SEM/EDX element X-ray maps of the Sanicro 28 steel coupon cross-section area. The heat treatment temperature 560 °C deposited with salt case 10.0 wt-% Cl, 20 wt-% melt

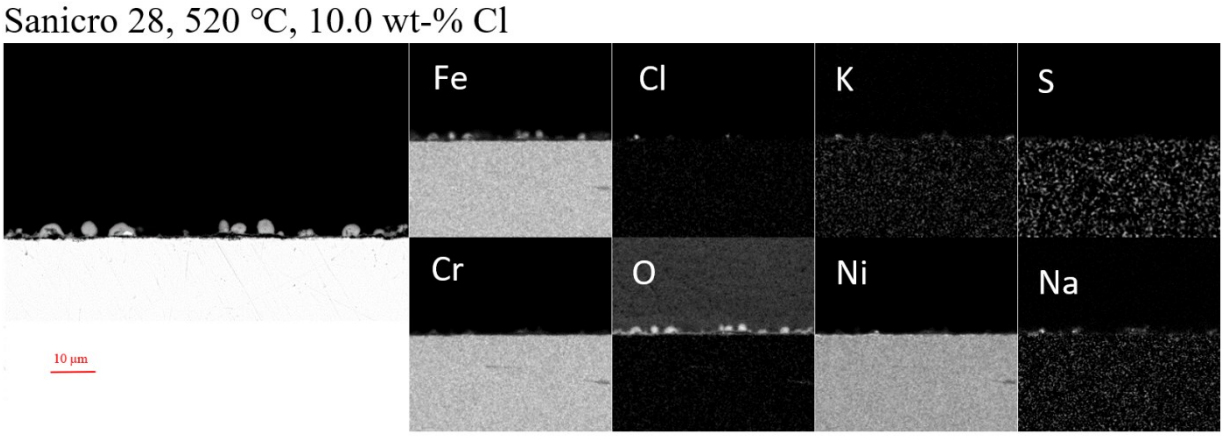

Figure 20. SEM/EDX element X-ray maps of the Sanicro 28 steel coupon cross-section area. The heat treatment temperature 520 °C deposited with salt case 10.0 wt-% Cl, no melt

Oxide layer distribution

Previous studies have shown that local corrosion is generally occurring for austenitic stainless steels that are similar to the stainless steel Sanicro 28 in this work (Loto, 2013). Local corrosion is considered to be one of the most destructive and insidious forms of corrosion. Talbot et al. highlighted the gravity of this damage, and this is because it causes tube failures even if the average corrosion attack on the rest of the surface is minor. (Talbot & Talbot, 2007) Localized corrosion attack is not visible when only observing mean oxide layer thickness, which complicates the prediction of corrosion of Sanicro 28.

The distribution curves for the Sanicro 28 steel type exposed to 560 °C are displayed in the graph in Figure 10. The distribution curves for the experiments with lower melt fractions (2-10

wt-%) formed a similar shape, typically consisting of a sharp at the beginning followed by a "tail" at the end of the curve. Whereas the distribution curve for the salt with the highest melt fraction, 10 wt-% Cl and ~20 wt-% melt, showed a more widely distributed curve, indicating a more uniform corrosion layer across the steel surface of Sanicro 28.

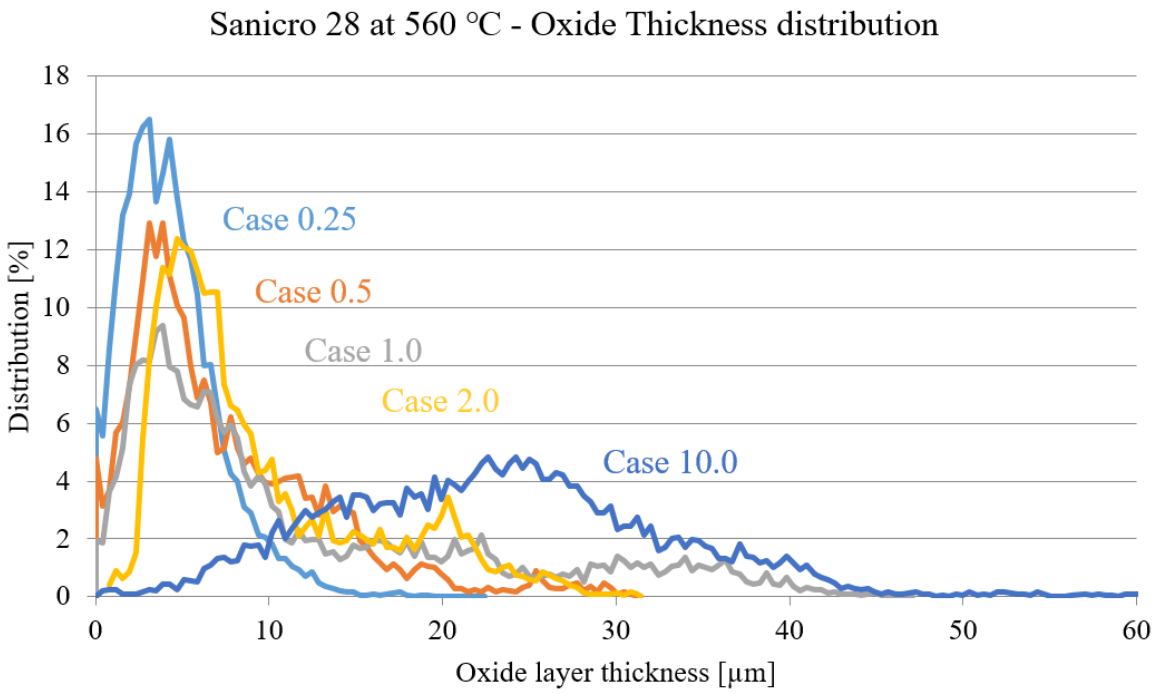

Figure 21. Corrosion layer thickness distribution of Sanicro 28 exposed to 560 °C for 168 h.

The mean value of corrosion layer thickness calculated from the panorama SEM images for Sanicro 28 indicates that only 20 wt-% molten phases cause significant corrosion. While the maximum value presented in Table 4 shows that there are areas where corrosion is more severe than what the mean value of oxide layer thickness would indicate. The determination of oxide layer thickness is an insufficient method to determine the severity of corrosion for Sanicro 28. Therefore, alternative methods are needed to map the corrosion of Sanicro 28 better.

The maximum value of oxide layer thickness for Sanicro 28 exceeds the limit for significant corrosion, 20 µm, for all cases above T_0. Additionally, the 90th percentile value was calculated for Sanicro 28 oxide layer thickness. The value of the 90th percentile means that 10 % of the data is above that value. The maximum value and 90th percentiles are presented in Table 8 and Table 9. Both maximum corrosion and percentile value for Sanicro 28 indicate that the limit for detectable corrosion occurs at a lower melt fraction.

Table 10. The maximum value of corrosion layer thickness.

Steel	Temperature (°C)	Case 0.25	Case 0.5	Case 1.0	Case 2.0	Case 10.0
10CrMo	560	70	84	126	226	257
	520	77	82	68	109	86
Sanicro 28	560	22	31	47	31	68
	520	14	7	17	9	13
Alloy 625	560	16	17	16	14	14
	520	-	7	-	7	9

Table 11 The 90th percentile value of corrosion layer thickness.

Steel	Temperature (°C)	Case 0.25	Case 0.5	Case 1.0	Case 2.0	Case 10.0
10CrMo	560	57	65	99	183	194
	520	70	70	44	88	67
Sanicro 28	560	8	15	30	20	36
	520	6	3	7	4	5
Alloy 625	560	5	3	5	2	6
	520	-	2	-	2	2

Based on the panorama SEM images and the distribution curves, local corrosion was typical for Sanicro 28 at the lower melt fractions, and as the melt fraction increased, a more uniform corrosion layer was formed. Figure 3 shows an example of how the corrosion layer thickness increases and becomes more uniform as the melt fraction increases in the deposit.

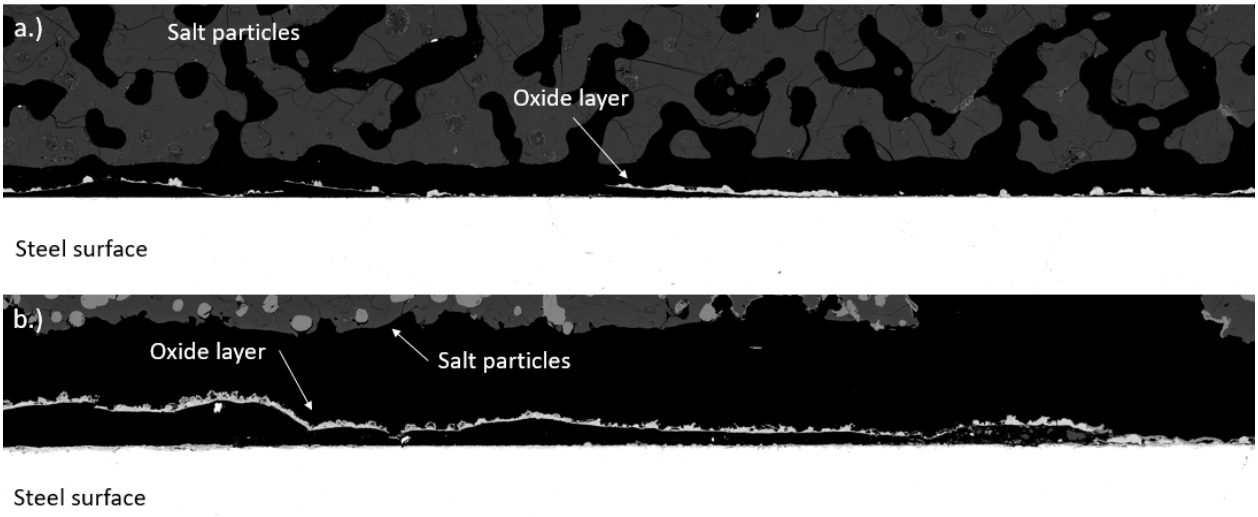

Figure 22 Image a.) represents the panorama SEM image of Sanicro 28 exposed to the salt case with 2.0 wt-% Cl, corresponding to ~10 wt-% molten phase at a temperature of 560 ℃ for 168 h and b.) represents the panorama SEM image of Sanicro 28 exposed to the salt case with 10.0 wt-% Cl, corresponding to ~20 wt-% molten phase at a temperature of 560 ℃ for 168 h.

Alloy 625

The nickel-based alloy, Alloy 625, had much stronger resistance to the molten salt deposit corrosion. The Ni-based alloy did not experience any adverse effects with the increased amount of molten phase. However, based on the X-ray diffraction images also for this alloy, a thin corrosion layer was detected at the highest melt fraction in this work; however, the oxide layer growth was completely negligible for this case.

The significantly higher corrosion resistance of nickel-based alloy, Alloy 625, is due to the high Ni content. A similar indication has previously been stated by Spiegel et al., where KCl particles were placed on iron, chromium, and nickel surfaces. The work concluded that nickel-based alloys are a more corrosion-resistant tubing material in biomass combustion environments compared to those with low nickel concentration. (Cha & Spiegel, 2006)

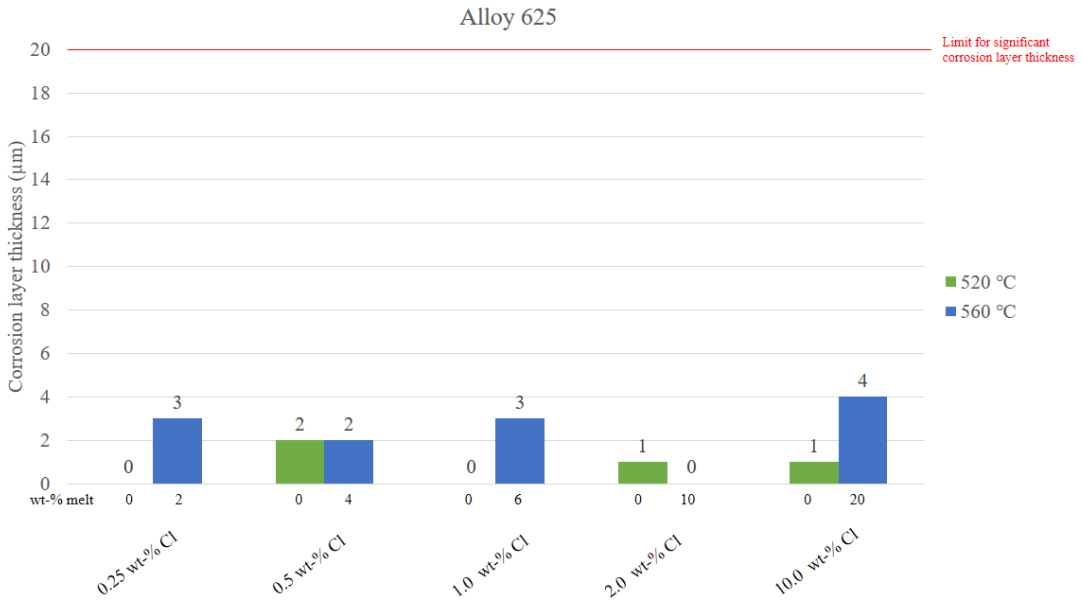

Elemental distribution in the oxide layer

The composition of the corrosion layers of Alloy 625 is presented in the table below. A small oxide layer consisting of iron oxide and chromium oxide is detected at the steel surface. Small amounts of nickel oxide also appear to be present in the oxide scale. A small amount of chlorine seems to have formed on the steel surface.

Alloy 625 560 °C 10 wt% Cl

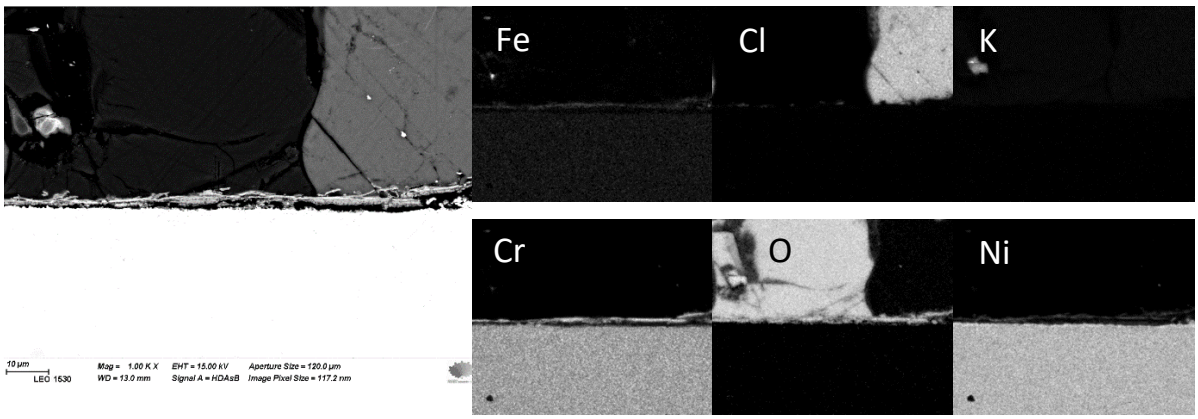

Figure 23 SEM/EDX element X-ray maps of the Alloy 625 coupon cross-section area. The heat treatment temperature 560 °C deposited with salt case 10.0 wt-% chlorine, which corresponds to ~20 wt-% melt.

Conclusions

The objective of this study was to obtain a better understanding of how the amount of melt impacts corrosion of superheater materials. Laboratory-scale corrosion tests were performed with five tailor-made synthetic alkali salts that were deposited on three steel materials. The composition of the salts was composed so that the first melting temperature (T_0) of the salts were the same, approximately 540 °C, while the melt fraction at 560 °C varied between the salts. Experiments were conducted above and below T_0 on two typical superheater materials (10CrMo9-10 and Sanicro 28) and one potential material, Alloy 625. The results showed that the amount of melt had a significant impact on the extent of corrosion.

The corrosion tendencies of the three steel types varied considerably, and the results showed that the composition of the steels had a great impact on corrosion resistance. In general, the corrosion was most severe for 10CrMo. The corrosion layer thickness was above 20 µm for all tested conditions. For Sanicro 28 corrosion ranged from 2-23 µm depending on the experimental conditions. In other words, corrosion of Sanicro 28 was generally on a lower level than 10CrMo. Alloy 625 showed least corrosion out of the three alloys tested. The corrosion was at maximum 4 µm corrosion when considering all tested conditions.

The amount of melt had a clear impact on corrosion layer thickness for 10CrMo9-10 and Sanicro 28, while for Alloy 625 the corrosion was generally low, and the amount of melt had essentially no impact on the corrosion layer thickness. The impact of the amount of melt varied somewhat between the steel grades; an increase in corrosion layer was observed at a higher melt fraction for Sanicro 28, whereas for 10CrMo9-10 the increase was observed to begin at a lower melt fraction (6 wt-%). However, the corrosion was severe in all tests with 10CrMo9-10, both below and above T_0. The low-alloy steel consists of high amounts of iron and a low amount of chromium, and as a consequence, this material is not protected by chromium-rich oxide.

Sanicro 28 withstood corrosion better than 10CrMo9-10, and no significant corrosion was observed up to 4 wt-% melt. The corrosion layer thickness was 5-7 µm. Low corrosion was detected for the tests with melt fractions of 6 wt-% and 10 wt-%, where the corrosion layer thickness was 10-12 µm. Significant corrosion for Sanicro 28 was detected at 20 wt-% melt fraction, where the corrosion layer thickness was 23 µm. While for the nickel-based alloy, Alloy 625, very little corrosion was observed with an increased amount of molten phase in the deposit. The nickel-based alloy showed high corrosion resistance even at a high amount of melt in the alkali salt deposit, highlighting the important role of nickel in the alloy for corrosion resistance.

The significantly higher corrosion resistance of nickel-based alloy, Alloy 625, is due to the high Ni content.

The salt mixtures in this study consisted of a variety of amounts of chlorine (0.25-10 wt-%) for the different salt cases. Interestingly, when comparing the corrosion layer thickness above and below T_0; corrosion layer thickness below T_0 did not increase even though the Cl-content in the deposit was increased – i.e., the corrosion did not appear to depend on the increasing Cl-content in the alkali salt. The result indicates that the presence of melt in the deposit significantly influences the corrosion. Highlighting the central role of the melting properties of the deposit in alkali-induced corrosion.

Considering the corrosion of Sanicro 28, the uneven corrosion behavior for Sanicro 28 makes it difficult to predict severity of corrosion. This is also due to the practical experience that the laboratory data does not one-to-one correspond to corrosion rates in boiler environments. Reporting mean oxide layer thickness is perhaps alone not sufficient to describe the full complexity of corrosion for Sanicro 28.

In summary, the results of this study imply that the amount of molten phase significantly increases the corrosion of 10CrMo9-10 and Sanicro 28. The steel composition has a significant impact on corrosion resistance. The work showed dramatic differences in the corrosion behavior between steels and the amount of molten phase in the salt deposits. The highest chloride contents in the tailor-made salt deposits are extreme case of Cl-content compared to the Scandinavian mills; the real chlorine content in the Scandinavian boilers is about 1 wt-% chlorine. However, this work provides some fundamental studies into how corrosion depends on the amount of molten phase. Further work on this topic could include studies on the impact of melt closer to T_0 since the temperature ranges used in this work is quite broad.

References

Adams, T. N., & Frederick, W. J. (1988). *Kraft recovery boiler physical and chemical processes*. American Paper Institute.

Adams, T. N., Frederick, W. J., & Hupa, M. (1997*). Kraft recovery boilers*. American Forest & Paper Association; Tappi Press.

Alan Buis. (2019). *The Atmosphere: Getting a Handle on Carbon Dioxide. NASA Global Climate Change and Global Warming: Vital Signs of the Planet*. https://climate.nasa.gov/

Backman, R., Hupa, M., & Uppstu, E. (1987). *Fouling and corrosion mechanisms in the recovery boiler superheater area.* Tappi Journal, 70(6), 123-127.

Bajpai, P. (2017). *Pulp and paper industry: chemical recovery*. Elsevier.

Bale, C. W., Bélisle, E., Chartrand, P., Decterov, S. A., Eriksson, G., Gheribi, A. E., Hack, K., Jung, I., Kang, Y., & Melançon, J. (2016). *Reprint of: FactSage thermochemical software and databases, 2010–2016*. Calphad, 55, 1-19.

Bankiewicz, D. (2012a). Corrosion behavior of boiler tube materials during combustion of fuels containing Zn and Pb.

Bhadeshia, H. K. D. H., & Honeycombe, R. W. K. (2006). *Steels: microstructure and properties (3rd ed.)*. Elsevier, Butterworth-Heinemann.

Cantatore, V., Olivas Ogaz, M. A., Liske, J., Jonsson, T., Svensson, J., Johansson, L., & Panas, I. (2019). *Oxidation driven permeation of Iron oxide scales by chloride from experiment guided first-principles modeling.* The Journal of Physical Chemistry C, 123(42), 25957-25966.

Cha, S. C., & Spiegel, M. (2006). *Local reactions of KCl particles with iron, nickel and chromium surfaces*. Materials and Corrosion, 57(2), 159-164.

Cheremisinoff, N. P., & Rosenfeld, P. E. (2010). *Chapter 6 - Sources of air emissions from pulp and paper mills.* In N. P. Cheremisinoff, & P. E. Rosenfeld (Eds.), Handbook of Pollution Prevention and Cleaner Production (pp. 179-259). William Andrew Publishing. https://doi.org/10.1016/B978-0-08-096446-1.10006-1

Cottis, R. A. (2010). *Basic concepts, high temperature corrosion* (4th ed ed.). Academic Press/Elsevier.

Enestam, S. (2011). *Corrosivity of hot flue gases in the fluidized bed combustion of recovered waste wood* https://abo.finna.fi/Record/abo.9911009893405972

Gjerde, D. T., Fritz, J. S., & Leonard, M. A. (1987). *Ion Chromatography*, 2nd Edn.: Hüthig, Heidelberg, 1987 (ISBN 3-7785-1207-2). Xi 283 Pp.Price DM 86 (US $45),

Goldstein, J., Newbury, D. E., Michael, J. R., Ritchie, N. W. M., Scott, J. H. J., & Joy, D. C. (2018). *Scanning electron microscopy and x-ray microanalysis* (Fourth edition ed.). Springer Science+Business Media, LLC.

Grabke, H. J., Reese, E., & Spiegel, M. (1995). *The effects of chlorides, hydrogen chloride, and sulfur dioxide in the oxidation of steels below deposits.* Corrosion Science, 37(7), 1023-1043.

Green, R. P., Hough, G., & Alkaline Pulping Committee. (1992). *Chemical recovery in the alkaline pulping processes* (3rd ed.). TAPPI Press.

Haaga, K., Laitinen, M., & Oy, K. P. (2002). *The experiences of the world's biggest recovery boiler in Yang Pu at Hainan Jinhai Pulp & Paper Co*. Kvaerner Power Oy,

Hansen, L. A., Nielsen, H. P., Frandsen, F. J., Dam-Johansen, K., Hørlyck, S., & Karlsson, A. (2000). *Influence of deposit formation on corrosion at a straw-fired boiler*. Fuel Processing Technology, 64(1), 189-209. https://doi.org/10.1016/S0378-3820(00)00063-1

Jose, P. D., Gupta, D. K., & Rapp, R. A. (1985*). Solubility of α-Al2 O 3 in Fused Na2 SO 4 at 1200 K*. Journal of the Electrochemical Society, 132(3), 735.

Kofstad, P. (1988*). High temperature corrosion*. Elsevier Applied Science.

Larsson, E. (2017*). The Corrosive Effect of Chlorine Containing Species on Waterwalls and Superheater Materials in Waste and Biomass-Fired Power Plants*. Chalmers University of Technology.

Lindberg, D., Backman, R., & Chartrand, P. (2007). *Thermodynamic evaluation and optimization of the (NaCl+Na2SO4+Na2CO3+KCl+K2SO4+K2CO3) system,* https://doi.org/10.1016/j.jct.2006.12.018 ".

Loto, R. T. (2013). *Pitting corrosion evaluation of austenitic stainless steel type 304 in acid chloride media.* J.Mater.Environ.Sci., 4(4), 448-459.

Mikkanen, P., Kauppinen, E. I., Pyykönen, J., Jokiniemi, J. K., Aurela, M., Vakkilainen, E. K., & Janka, K. (1999). *Alkali salt ash formation in four Finnish industrial recovery boilers*. Energy & Fuels, 13(4), 778–795.

Nielsen, H. P., Frandsen, F. J., Dam-Johansen, K., & Baxter, L. L. (2000). *The implications of chlorine-associated corrosion on the operation of biomass-fired boilers.* Progress in Energy and Combustion Science, 26(3), 283-298. https://doi.org/10.1016/S0360-1285(00)00003-4

Niu, Y., & Tan, H. (2016). *Ash-related issues during biomass combustion: Alkali-induced slagging, silicate melt-induced slagging (ash fusion), agglomeration, corrosion, ash utilization, and related countermeasures.* Progress in Energy and Combustion Science, 52, 1-61.

Pachauri, R. K., & Reisinger, A. (2008). *Climate change 2007. Synthesis report*. Contribution of Working Groups I, II and III to the fourth assessment report.

Pettersson, C., Johansson, L., & Svensson, J. (2008). *The influence of small amounts of KCl (s) on the initial stages of the corrosion of alloy Sanicro 28 at 600° C*. Oxidation of Metals, 70(5), 241-256.

Pettersson, J., Asteman, H., Svensson, J., & Johansson, L. (2005). *KCl induced corrosion of a 304-type austenitic stainless steel at 600 C; the role of potassium*. Oxidation of Metals, 64(1), 23-41.

Rapp, R. A. (2002*). Hot corrosion of materials: a fluxing mechanism?* Corrosion Science, 44(2), 209-221.

Rapp, R. A. (1989). Hot Corrosion of Materials. Studies in Inorganic Chemistry, 9, 291-329. https://doi.org/10.1016/B978-0-444-88534-0.50016-3

Ropo, M., Kokko, K., Airiskallio, E., Punkkinen, M. P. J., Hogmark, S., Kollár, J., Johansson, B., & Vitos, L. (2011). *First-principles atomistic study of surfaces of Fe-rich Fe–Cr.* Journal of Physics: Condensed Matter, 23(26), 265004.

Salmenoja, K. (1999). *Thermogravimetric studies on the oxidation and corrosion of metals and alloys in HCl containing atmospheres*. Åbo Akademi.

Salmenoja, K. (2000). *Field and laboratory studies on chlorine-induced superheater corrosion in boilers fired with biofuels*

Sandvik Sanicro 28. https://www.materials.sandvik/en/materials-center/material-datasheets/tube-and-pipe-seamless/sanicro-28/ (accessed on May 3, 2021)

Shinata, Y. (1987). *Accelerated oxidation rate of chromium induced by sodium chloride. Oxidation of Metals*, 27(5–6), 315-332. 10.1007/BF00659274

Skrifvars, B., Backman, R., Hupa, M., Salmenoja, K., & Vakkilainen, E. (2008). *Corrosion of superheater steel materials under alkali salt deposits Part 1: The effect of salt deposit composition and temperature.* Corrosion Science, 50(5), 1274-1282.

Skrifvars, B., Westén-Karlsson, M., Hupa, M., & Salmenoja, K. (2010). *Corrosion of super-heater steel materials under alkali salt deposits. Part 2: SEM analyses of different steel materials*. Corrosion Science, 52(3), 1011-1019.

Soodakattilayhdistys. (2009*). 45 years recovery boiler co-operation in Finland. Paper presented at the International Recovery Boiler Conference*,

Special material corporation. (2013). specialmetals.com, https://www.specialmetals.com/assets/smc/documents/alloys/inconel/inconel-alloy-625.pdf (accessed on May 3, 2021)

Spiegel, M. (1999). *Salt melt induced corrosion of metallic materials in waste incineration plants*. Materials and Corrosion, 50(7), 373-393.

Suomen standardisoimisliitto. (2008*). Seamless steel tubes for pressure purposes. Technical delivery conditions. Part 2: Non-alloy and alloy steel tubes with specified elevated temperature properties. Suomen standardisoimisliitto.* (accessed on May 3, 2021)

Talbot, D. E. J., & Talbot, J. D. R. (2007). Corrosion science and technology (2nd ed ed.). Taylor & Francis.

Tran, H., & Vakkilainen, E. K. (2008). *The kraft chemical recovery process*. Tappi Kraft Pulping Short Course, 1-8.

Trethewey, K. R., & Chamberlain, J. (1995). Corrosion for science and engineering (2. ed.). Longman.

Verrill, C. L. (1992). *Inorganic aerosol formation during black liquor drop combustion. Inorganic Aerosol Formation during Black Liquor Drop Combustion*,

Werkelin, J. (2008*). Ash-forming elements and their chemical forms in woody biomass fuels.*

Wong, K. V. (2015). Climate Change. Momentum Press.

Zahs, A., Spiegel, M., & Grabke, H. J. (2000). *Chloridation and oxidation of iron, chromium, nickel and their alloys in chloridizing and oxidizing atmospheres at 400–700 C*. Corrosion Science, 42(6), 1093-1122.

Appendices

Appendix 1. Distribution curves

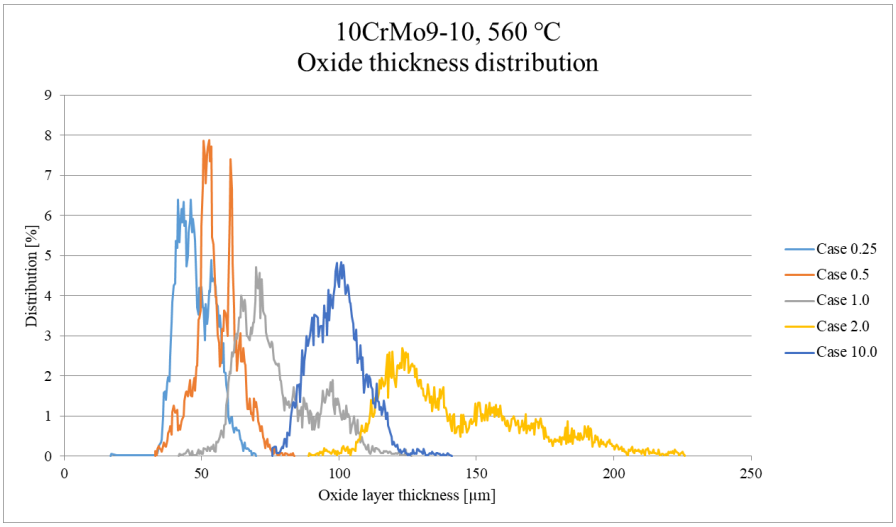

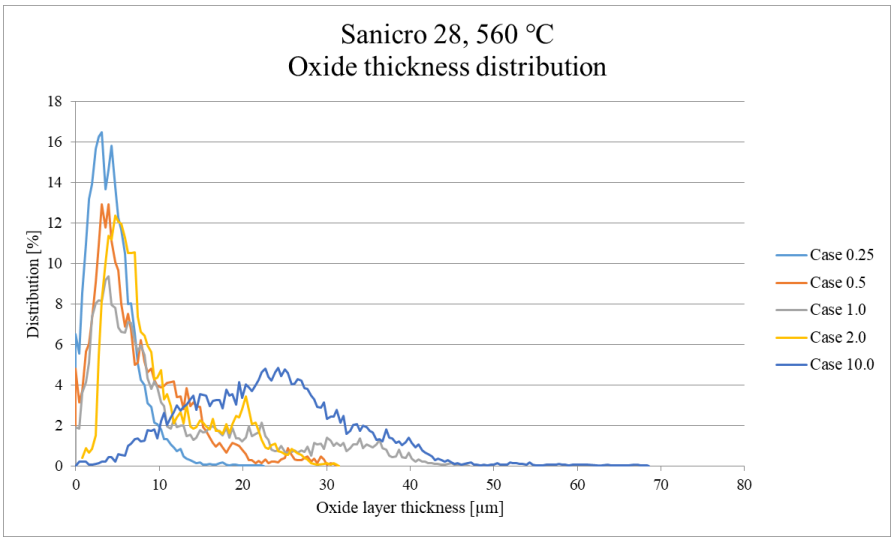

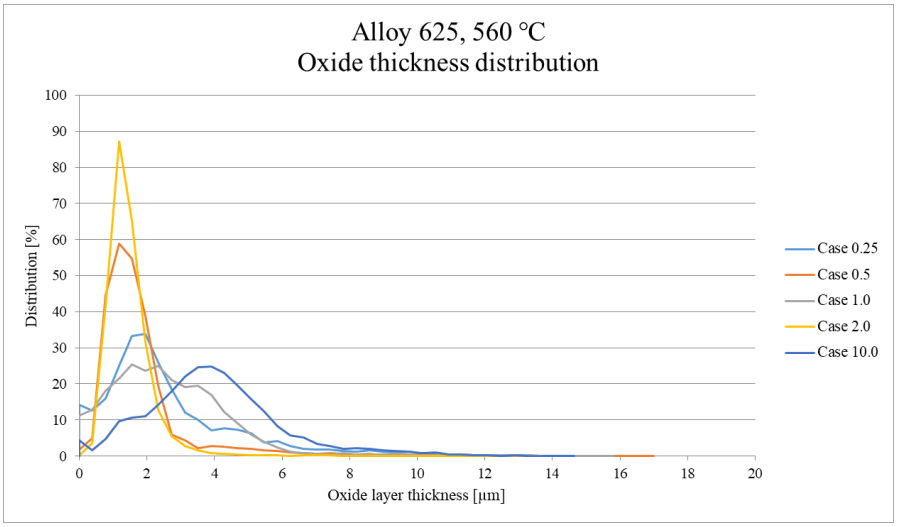

Appendix B. Elemental maps

10CrMo9-10

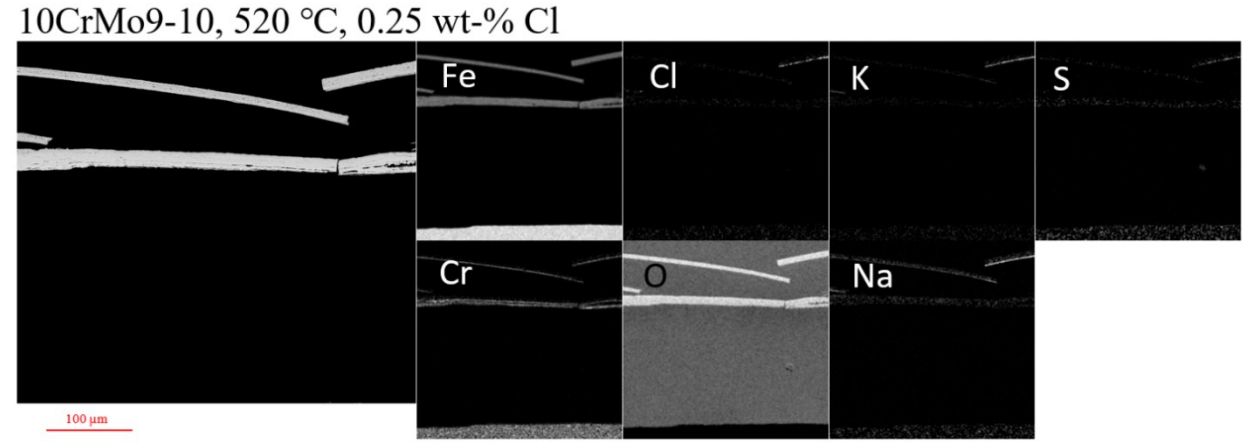

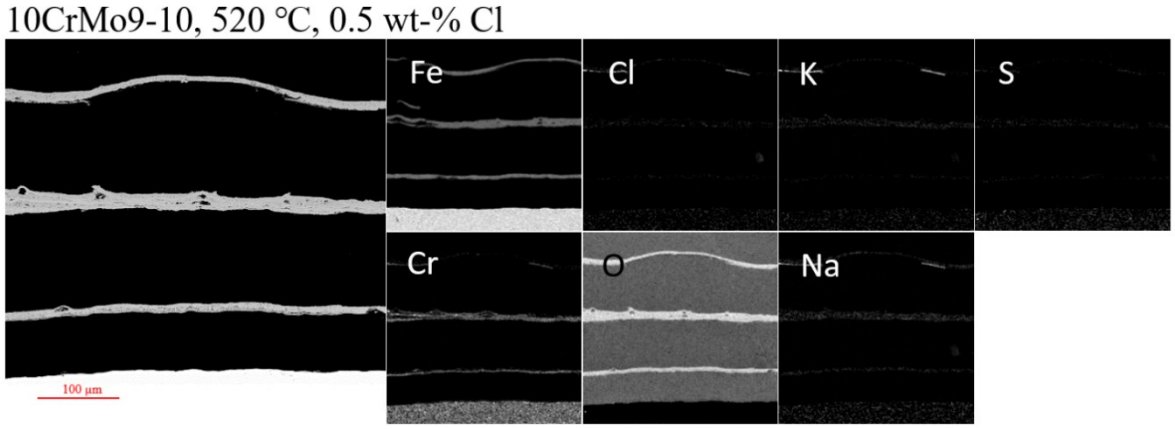

10CrMo9-10, 520 °C, 1.0 wt-% Cl

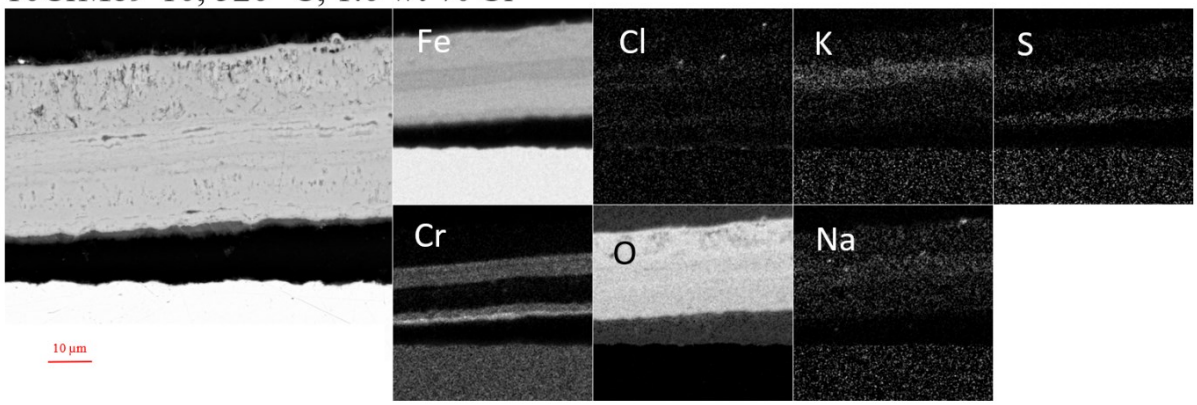

10CrMo9-10, 520 °C, 2.0 wt-% Cl

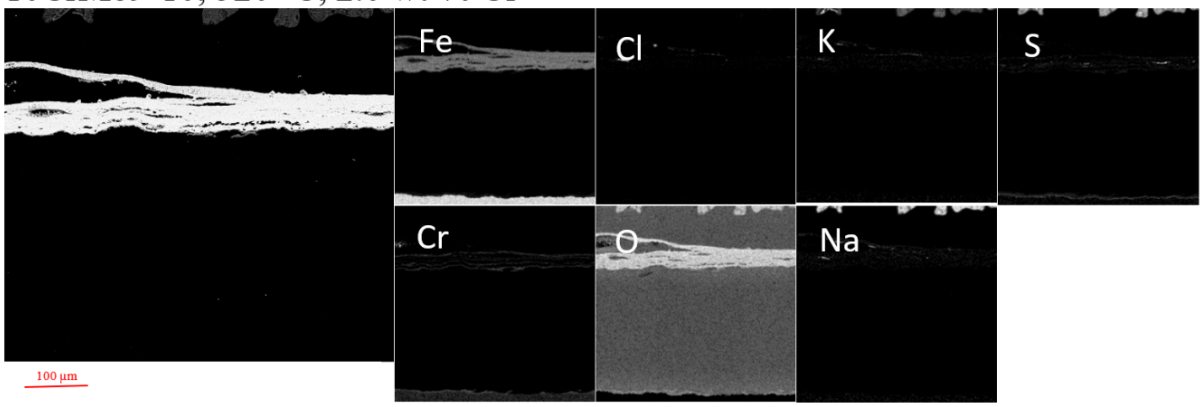

10CrMo9-10, 520 °C, 10.0 wt-% Cl

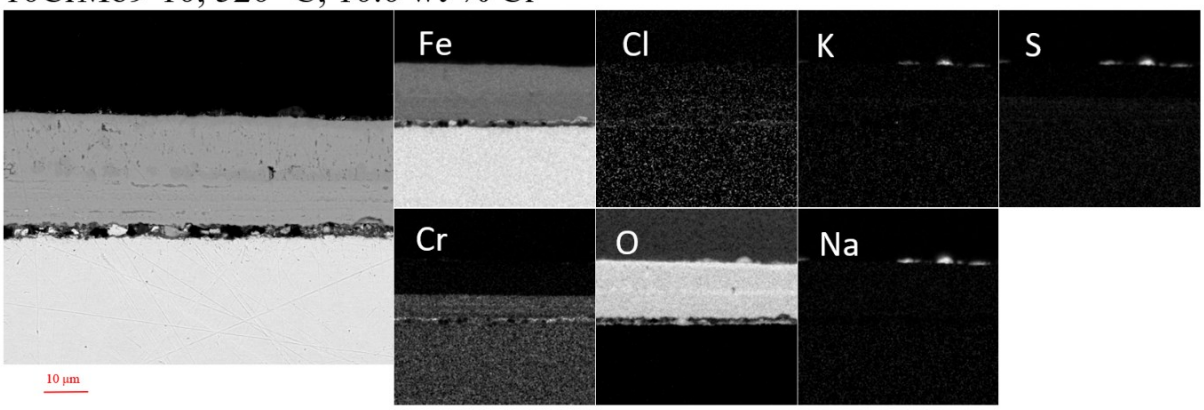

10CrMo9-10, 560 °C, 0.25 wt-% Cl, ~2 wt-% melt

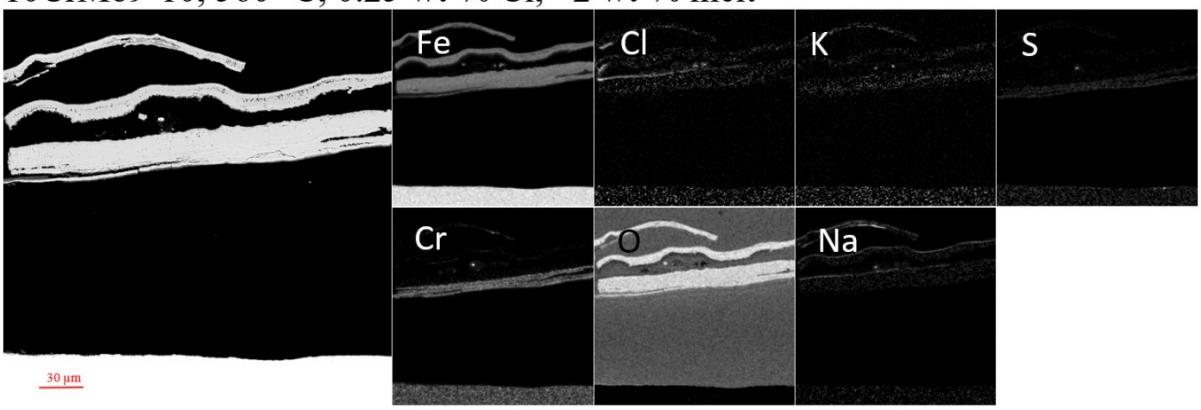

10CrMo9-10, 560 °C, 0.5 wt-% Cl, ~ 4 wt-% melt

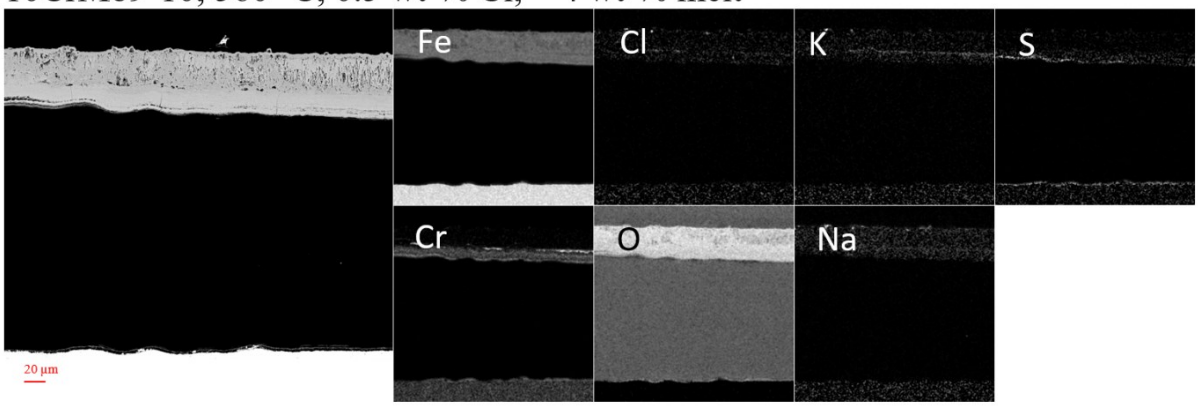

10CrMo9-10, 560°C, 1.0 wt-% Cl, ~ 6 wt-% melt

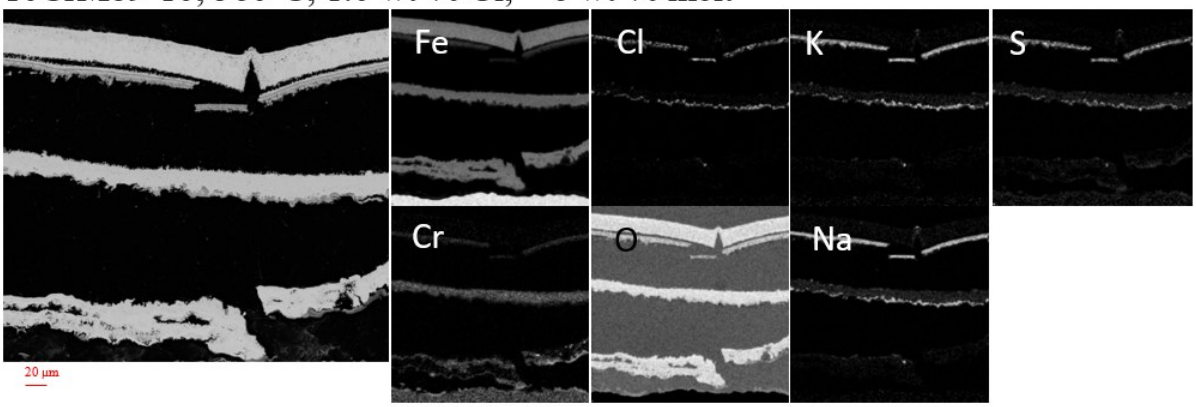

10CrMo9-10, 560 °C, 2.0 wt-% Cl, ~ 10 wt-% melt

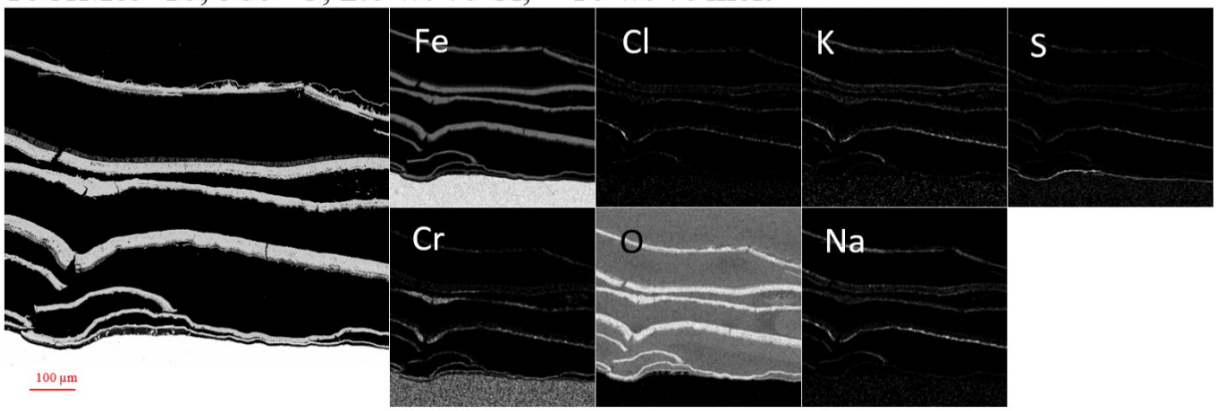

10CrMo9-10, 560 °C, 10.0 wt-% Cl, ~ 20 wt-% melt

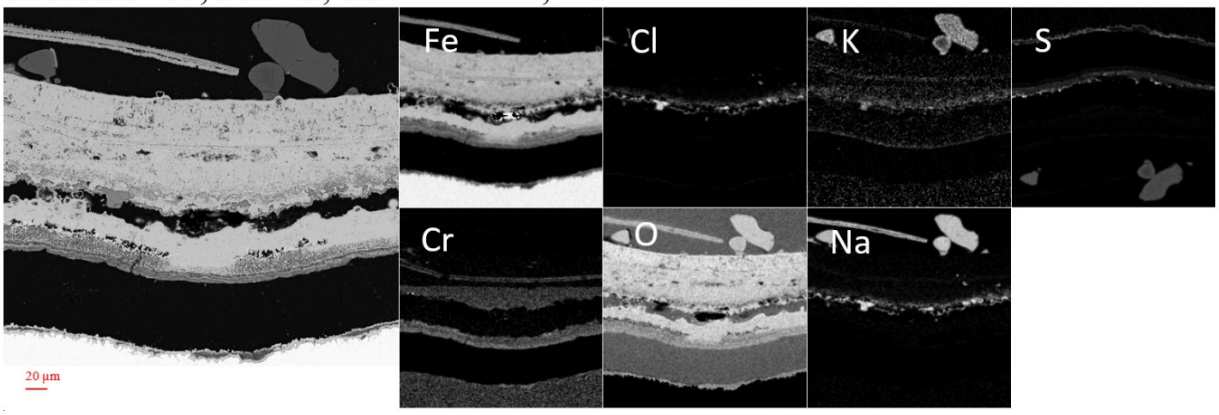

Sanicro 28

Sanicro 28, 520 °C, 0.25 wt% Cl

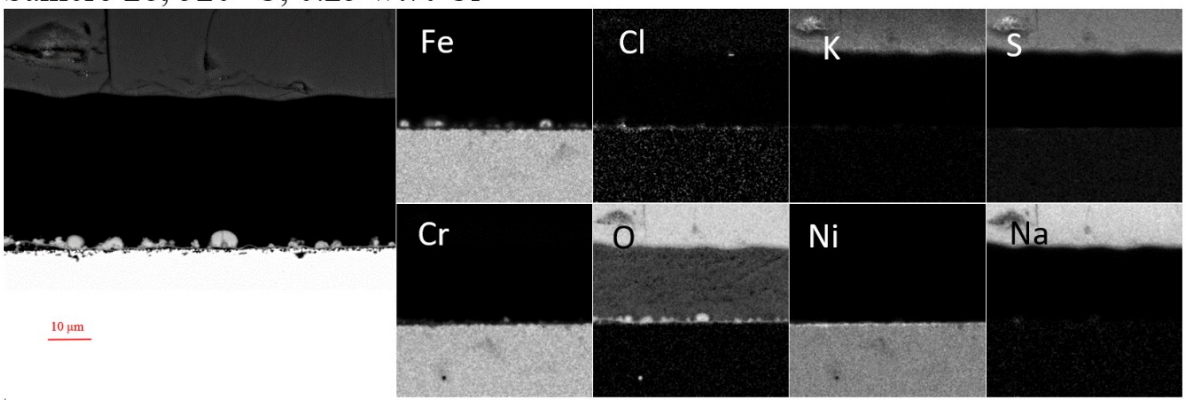

Sanicro 28, 520 °C, 0.5 wt-% Cl

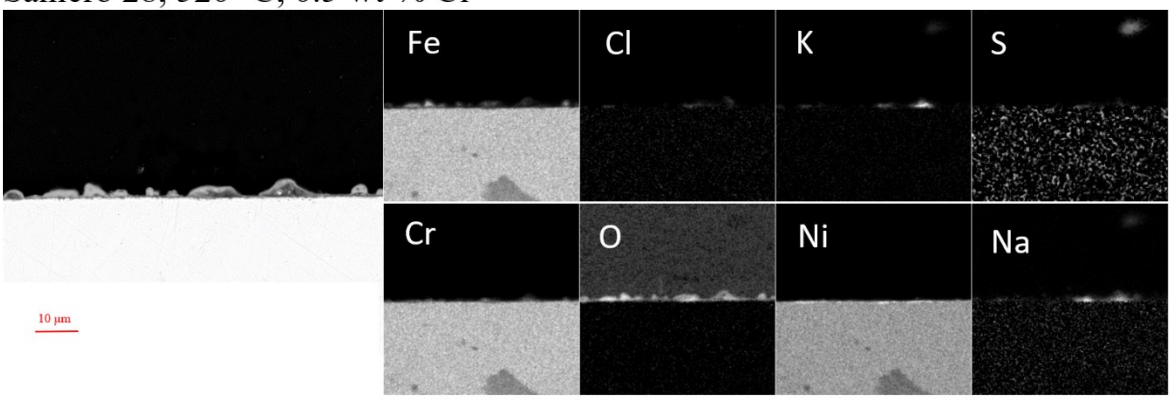

Sanicro 28, 520 °C, 1.0 wt-% Cl

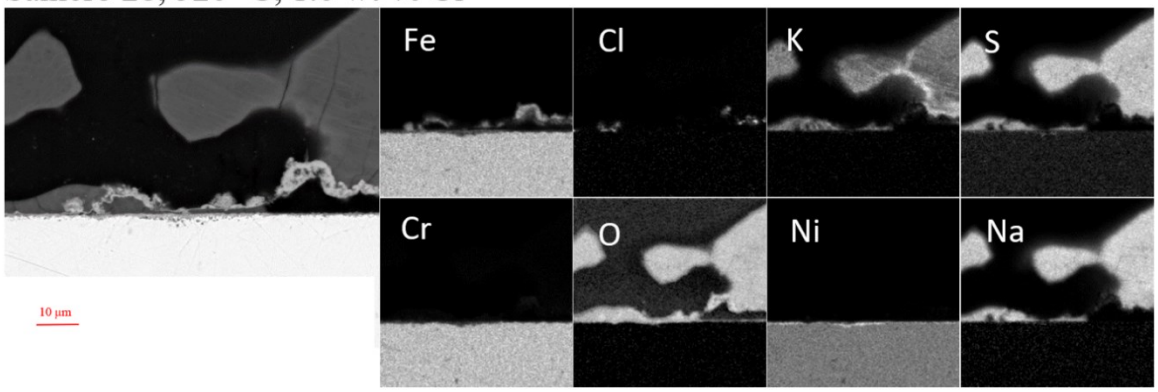

Sanicro 28, 520 °C, 2.0 wt-% Cl

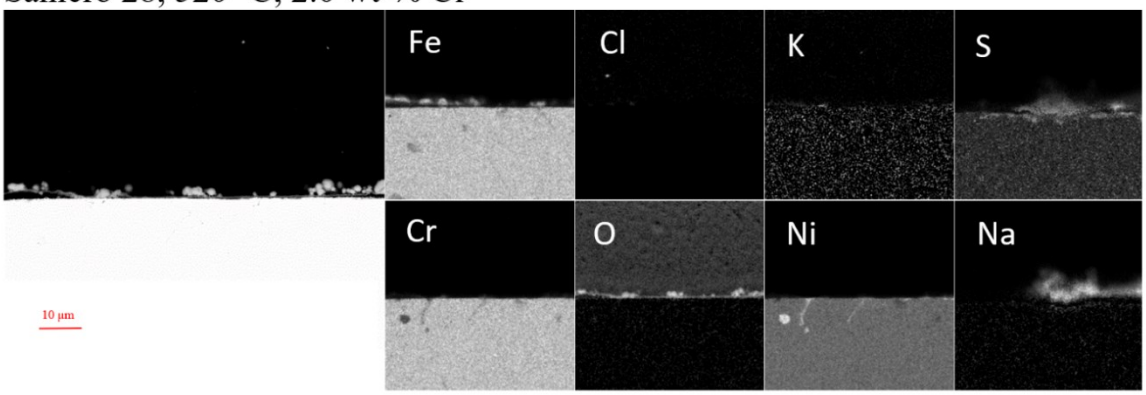

Sanicro 28, 520 °C, 10.0 wt-% Cl

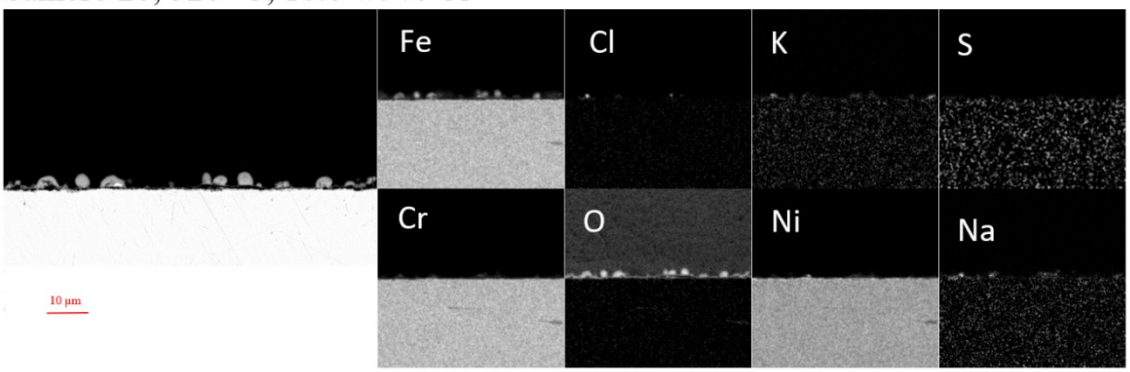

Sanicro 28, 560 °C, 0.25 wt-% Cl, ~2 wt-% melt

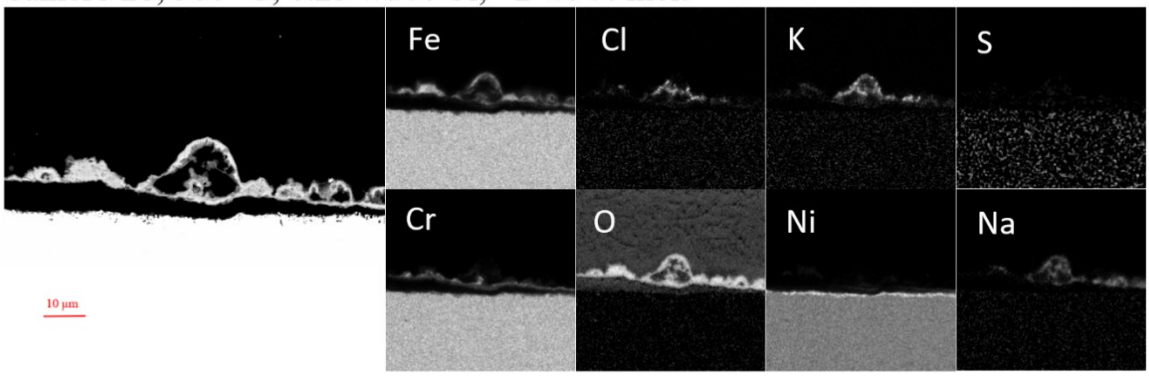

Sanicro 28, 560 °C, 0.5 wt-% Cl, ~ 4 wt-% melt

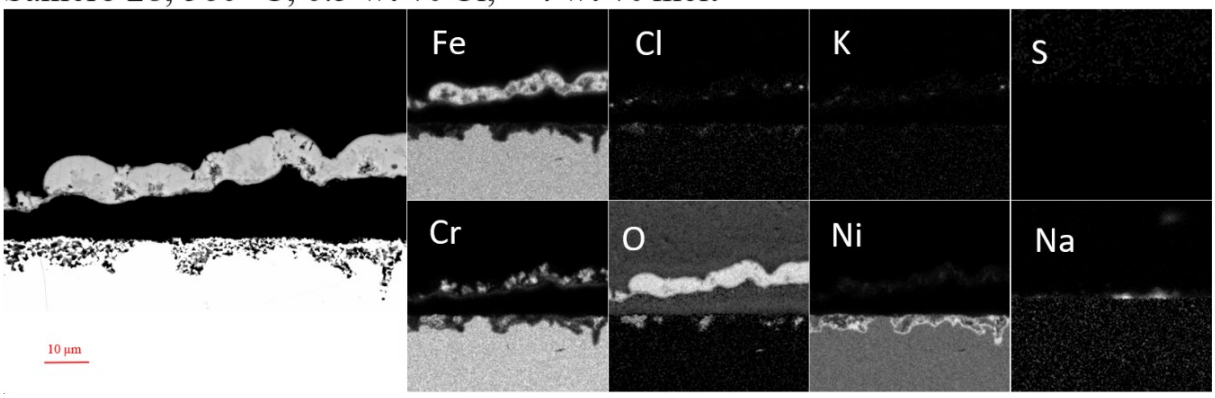

Sanicro 28, 560 °C, 1.0 wt-% Cl, ~ 6 wt-% melt

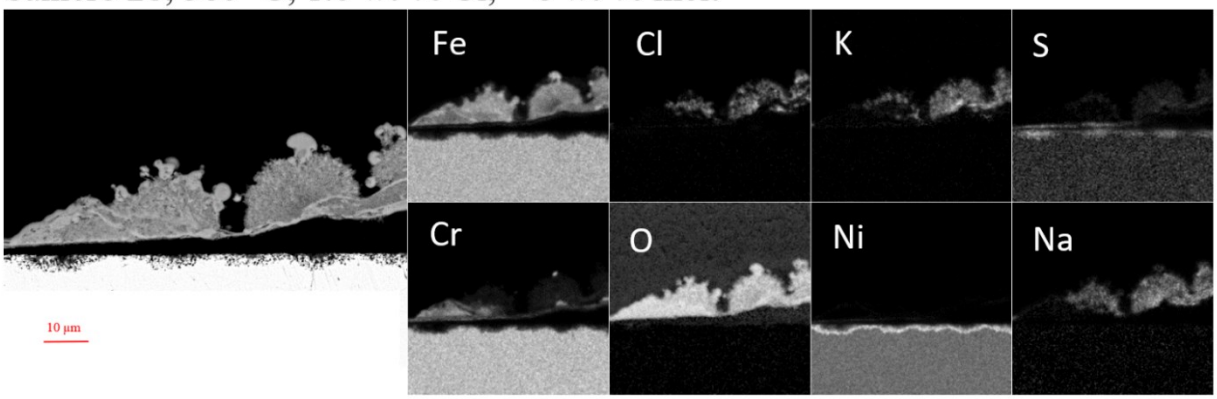

Sanicro 28, 560 °C, 2.0 wt-% Cl, ~10 wt-% melt

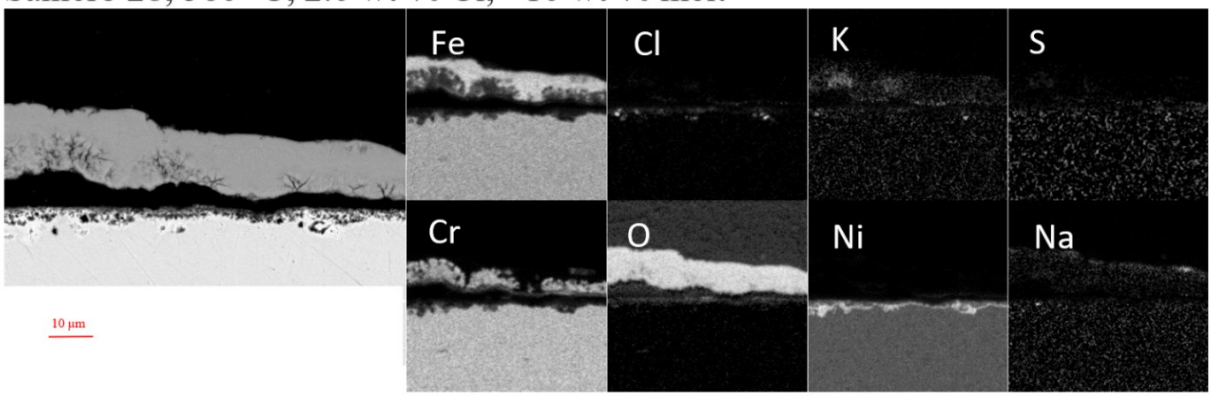

Sanicro 28, 560 °C, 10.0 wt-% Cl, ~ 20 wt-% melt

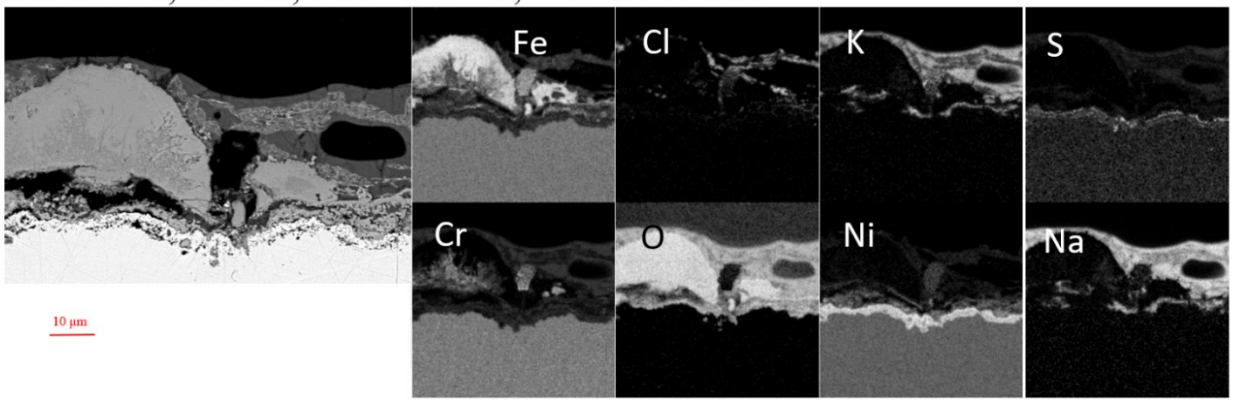

Alloy 625

Alloy 625, 520 °C, 0.25 wt-% Cl

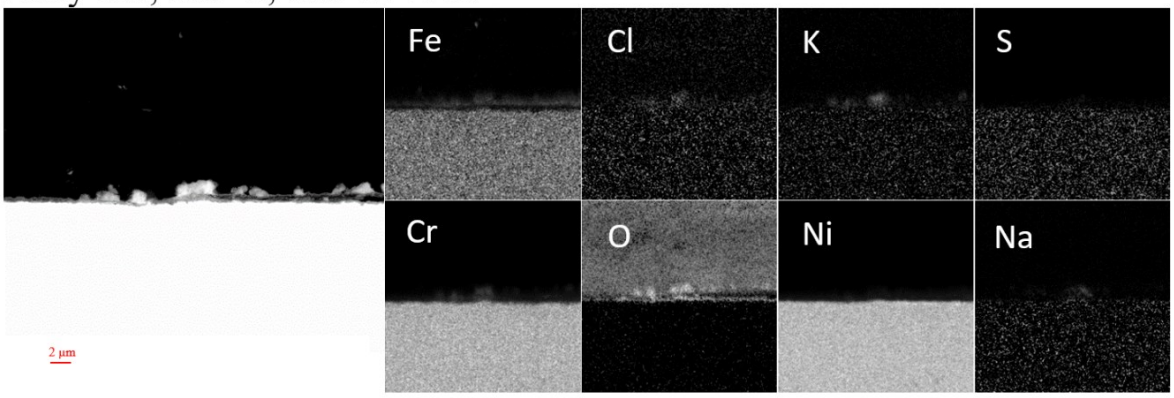

Alloy 625, 520 °C, 0.5 wt-% Cl

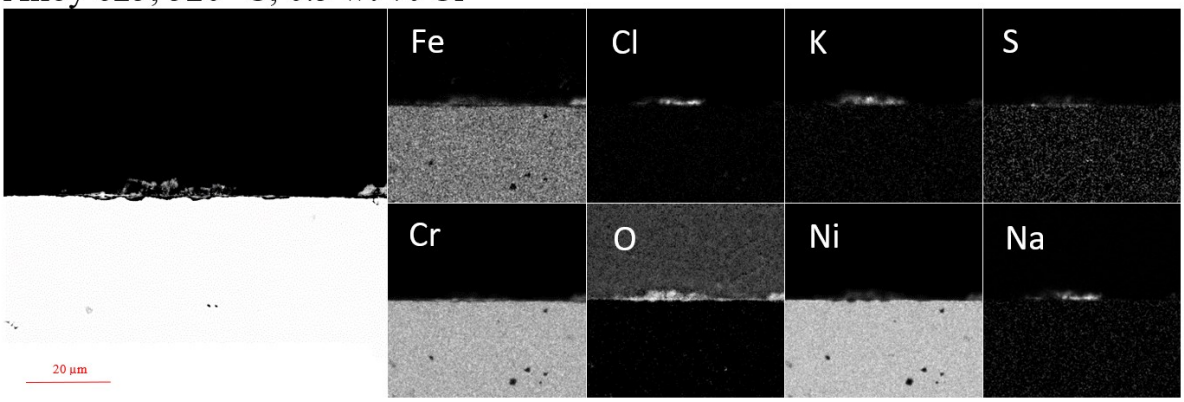

Alloy 625, 520 °C, 1.0 wt-% Cl

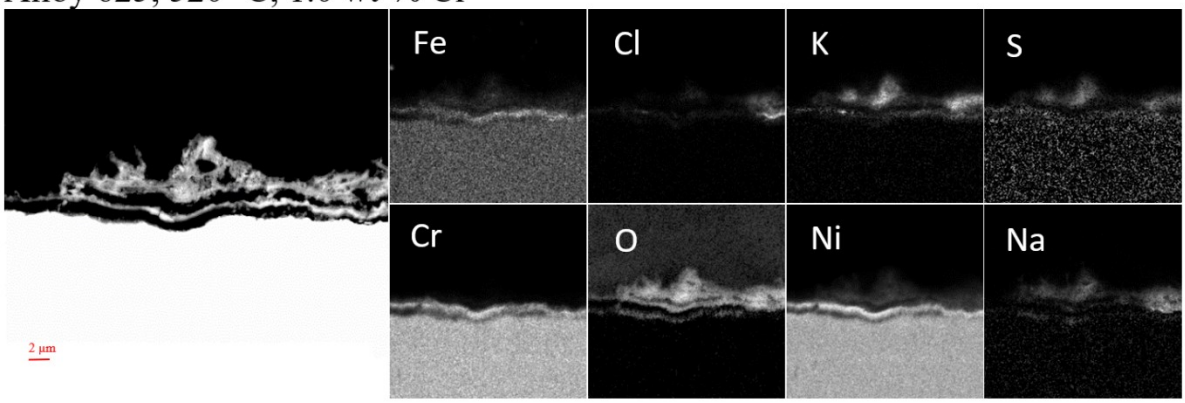

Alloy 625, 520 °C, 2.0 wt-% Cl

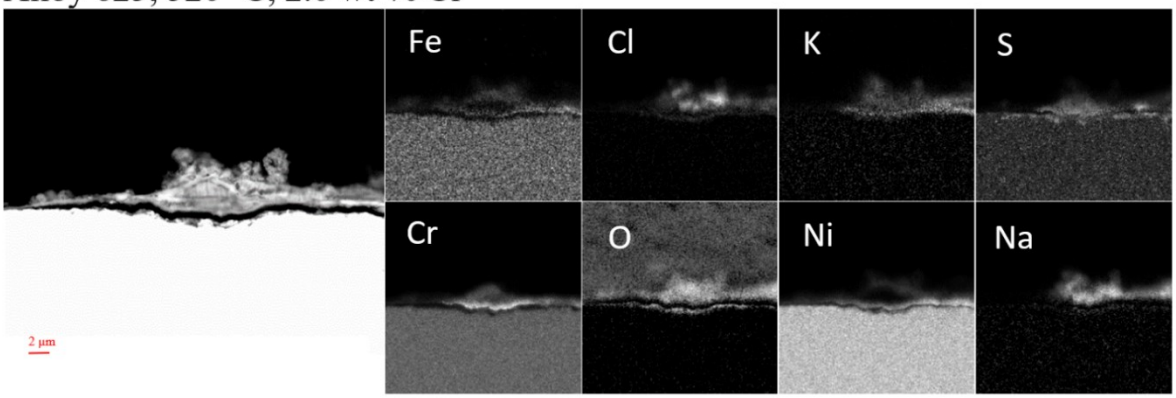

Alloy 625, 520 °C, 10.0 wt-% Cl

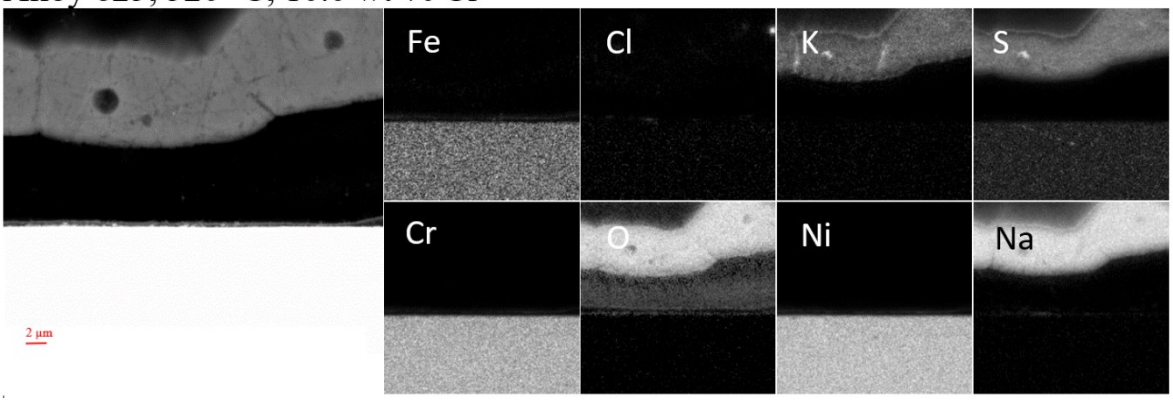

Alloy 625, 560 °C, 0.25 wt-% Cl, ~ 2 wt-% melt

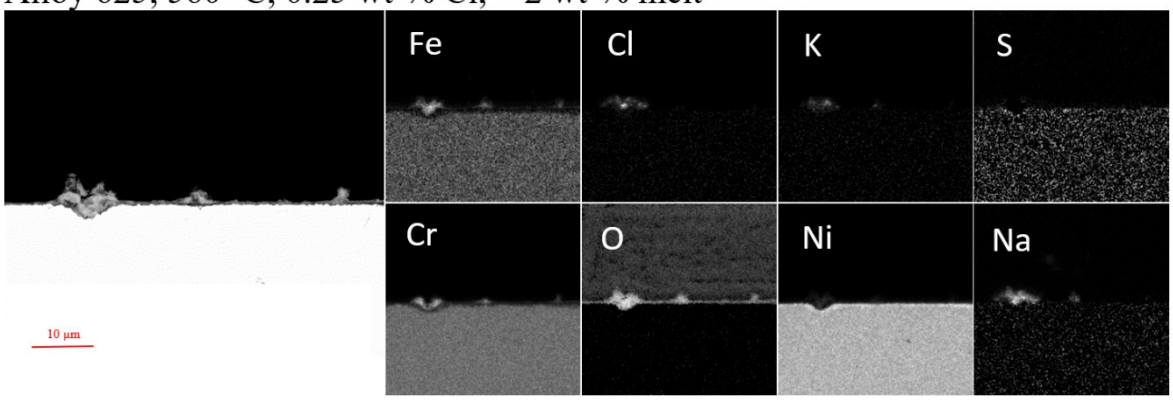

Alloy 625, 560 °C, 0.5 wt-% Cl, ~ 4 wt-% melt

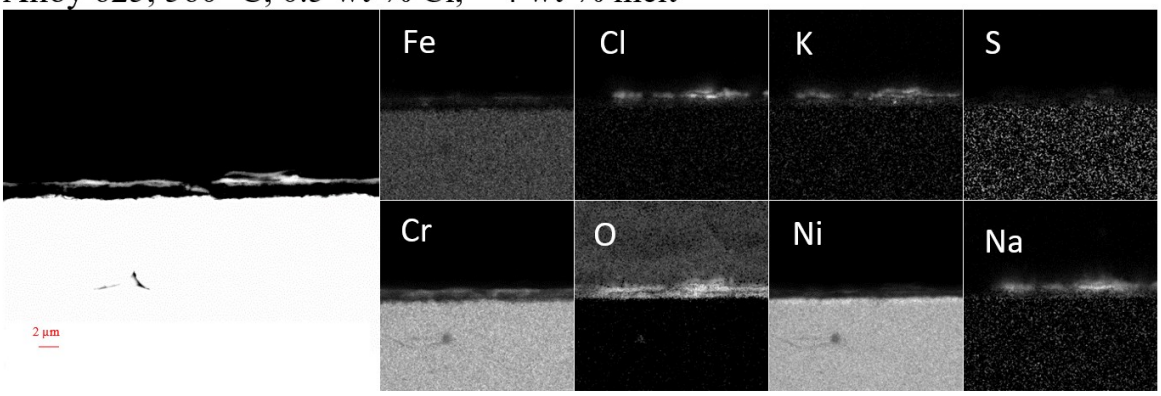

Alloy 625, 560 °C, 1.0 wt-% Cl, ~ 6 wt-% melt

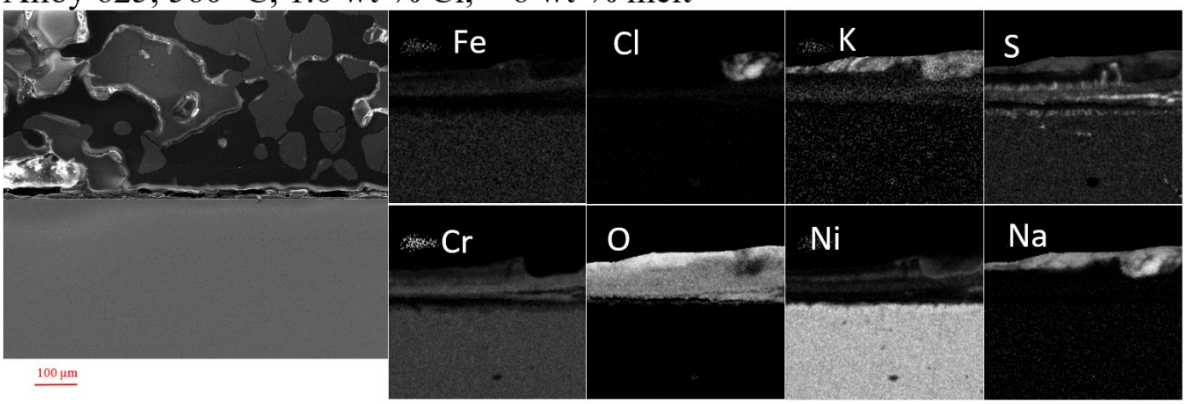

Alloy 625, 560 °C, 2.0 wt-% Cl, ~ 10 wt-% melt

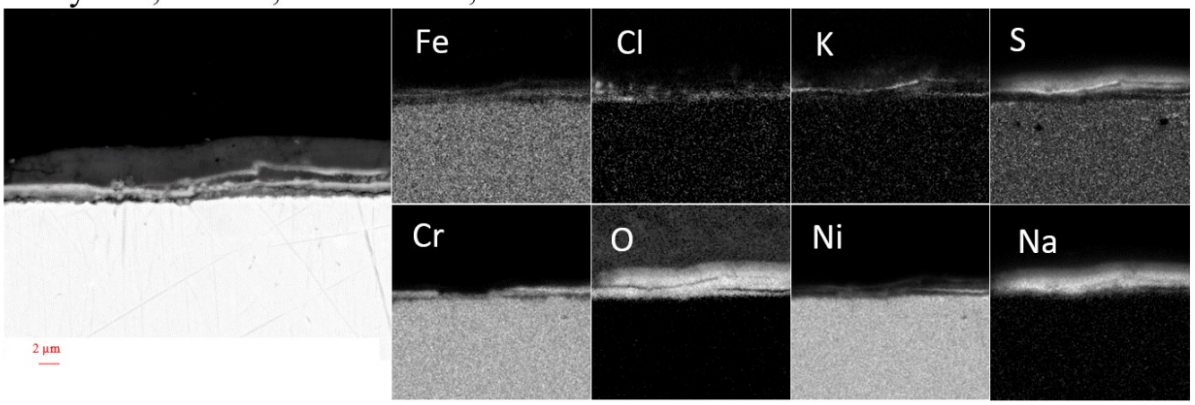

Alloy 625, 560 °C, 10.0 wt-% Cl, ~ 20 wt-% melt

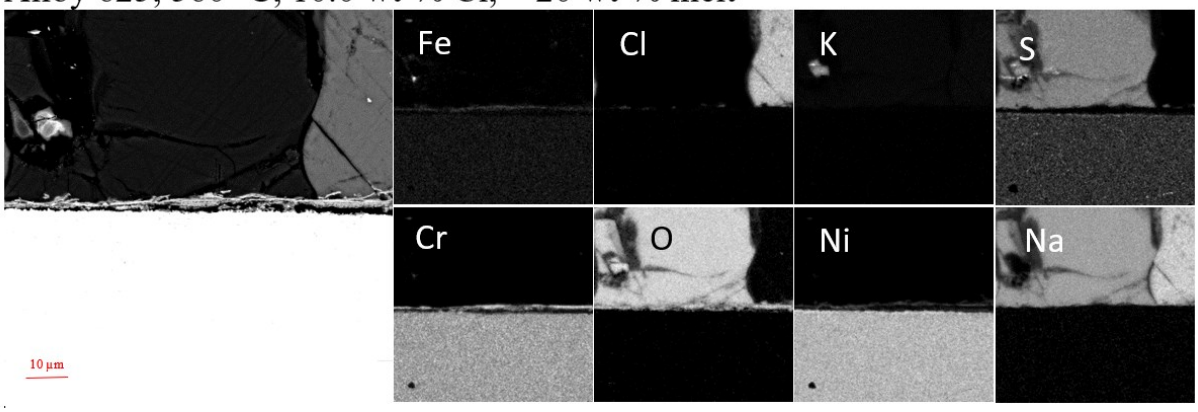

Appendix C. Data Tables

90th percentile value of oxide layer thickness

Steel	Temperature (°C)	Case 0.25	Case 0.5	Case 1.0	Case 2.0	Case 10.0
10CrMo9	560	57	65	99	183	194
	520	70	70	44	88	67
Sanicro 28	560	8	15	30	20	36
	520	6	3	7	4	5
Alloy 625	560	5	3	5	2	6
	520	-	2	-	2	2

The maximum value of oxide layer thickness

Steel	Temperature (°C)	Case 0.25	Case 0.5	Case 1.0	Case 2.0	Case 10.0
10CrMo	560	70	84	126	226	257
	520	77	82	68	109	86
Sanicro 28	560	22	31	47	31	68
	520	14	7	17	9	13
Alloy 625	560	16	17	16	14	14
	520	-	7	-	7	9